Self-Correcting Gottesman-Kitaev-Preskill Qubit and Gates in a Driven-Dissipative Circuit

Frederik Nathan,[1,2,*] Liam O'Brien,[2] Kyungjoo Noh,[3] Matthew H. Matheny,[3]
Arne L. Grimsmo,[3] Liang Jiang,[3,4] and Gil Refael[2,3]

[1] *NNF Quantum Computing Programme, Niels Bohr Institute, University of Copenhagen, Denmark*
[2] *Department of Physics and Institute for Quantum Information and Matter, California Institute of Technology, Pasadena, California 91125, USA*
[3] *AWS Center for Quantum Computing, Pasadena, California, 91125, USA*
[4] *Pritzker School of Molecular Engineering, The University of Chicago, Chicago, Illinois 60637, USA*

(Received 18 June 2024; revised 10 April 2025; accepted 9 July 2025; published 17 September 2025)

We show that a self-correcting Gottesman-Kitaev-Preskill (GKP) qubit can be realized with a high-impedance LC circuit coupled to a resistor and a Josephson junction via a controllable switch. When activating the switch in a particular stepwise pattern, the resonator relaxes into a subspace of GKP states that encode a protected qubit. Under continued operation, the resistor dissipatively error corrects the qubit against bit flips and decoherence by absorbing noise-induced entropy. We show that this leads to an exponential enhancement of the coherence time (T_1 and T_2), even in the presence of extrinsic noise, imperfect control, and device-parameter variations. We show that the qubit supports exponentially robust single-qubit Clifford gates, implemented via appropriate control of the switch, and readout and/or initialization via supercurrent measurement. The self-correcting properties of the qubit allow it to operate at approximately 1-K temperatures and resonator Q factors down to approximately 1000 for realistic parameters, and make it amenable to parallel control through global control signals. We discuss how the effects of quasiparticle poisoning—potentially, though not necessarily, a limiting factor—might be mitigated. We finally demonstrate that a related device supports a self-correcting magic T gate.

DOI: 10.1103/ykqb-m52z

I. INTRODUCTION

Quantum error correction is a crucial element in quantum computing, due to the inevitability of noise from, e.g., uncontrolled degrees of freedom, imperfect control, or fluctuations of device parameters [1–7]. Many approaches—such as surface codes—rely on *active correction*, which eliminates noise-induced entropy via readout and feedback [6–8]. Requirements for rapid readout, extensive control, and complex device architectures make the scalability of these approaches a significant challenge [7,9,10]. On the other hand, classical bits are often intrinsically stable due to *dissipation* [11,12]: in a magnetic hard disk, for example, noise-induced magnetic fluctuations are damped dissipatively before they accumulate to generate bit flips, leading to extreme robustness. Similarly harnessing dissipation for quantum error correction is a challenging, but desirable, goal [13–25].

Here, we propose an architecture for a dissipatively error-corrected qubit. The device consists of an LC resonator with impedance close to $h/2e^2 \approx 12.91$ kΩ, connected to a Josephson junction and a dissipative element through a controllable switch, which is activated via a stepwise protocol [Fig. 1(a)]. Quantum information is encoded in a thermal ensemble of generalized Gottesman-Kitaev-Preskill (GKP) states [26] (for details, see Sec. II and Fig. 2), and can be accessed and initialized via the Josephson-junction supercurrent. When the Josephson energy is larger than temperature and LC frequency, the qubit enters a regime of *dissipative error correction* (DEC), where noise-induced fluctuations are damped dissipatively without affecting the encoded information. Thereby, the resistor error corrects the qubit against bit flip *and* dephasing.

Our simulations show that DEC can leads to exponential increase of the coherence time that can extend beyond 10^6 oscillator cycles, even with extrinsic charge or flux noise present [Figs. 1(b) and 1(c)]. We confirm this exponential scaling analytically [Eq. (9)]. Its self-correcting properties

---

[*] Contact author: frederik.nathan@nbi.ku.dk

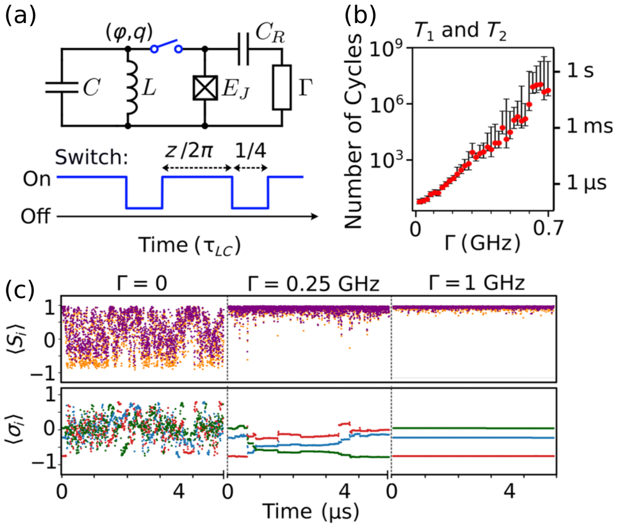

FIG. 1. The self-correcting GKP qubit. (a) The circuit diagram and protocol, where z is an integer and τ_{LC} is the oscillation period of the LC resonator. (b) The simulated qubit lifetime with extrinsic charge noise (strength $10^{-12}\, e^2/\text{Hz}$; see Sec. VII B), versus the resistor-induced loss rate, Γ [see Eq. (11)], for parameters $L = 10\ \mu\text{H}$, $C = 60$ fF, $z = 2$, and $E_J/h = 200$ GHz and resistor temperature $T = 40$ mK. The data points are obtained via averaging over 50–100 universal Lindblad equation (ULE) trajectories, with the error bars indicating the 95% confidence interval from bootstrap resampling. Note that bit flip and dephasing appear symmetrically in the protocol, implying that the relaxation and coherence times are *identical*: $T_1 = T_2$. (c) Expectations of GKP stabilizers S_1 and S_2 (purple and orange) and logical operators σ_x, σ_y, and σ_z (red, blue, and green) [see Eqs. (1), (3)] for individual randomly selected ULE trajectories at 3 values of Γ.

give the qubit finite tolerance for manufacturing and control imperfections, making the qubit amenable to parallel control through global control signals and, potentially, calibration-free operation. Additionally, the self-correcting properties allow the qubit to operate at relatively high temperatures (approximately 1 K) with imperfect resonators ($Q \sim 1000$) for realistic circuit parameters (see also Table I below).

DEC protects the qubit against phase-space local noise, generated by finite-order polynomials of mode quadratures. This generic class of noise includes flux and charge noise, along with uncontrolled deviations of device parameters and control signals. Notably, quasiparticle-poisoning events may fall outside this category and hence potentially—though not necessarily—provide a limiting factor for the stability of the qubit. We discuss possible consequences of quasiparticle poisoning and mitigation strategies in Sec. IX A below.

Interestingly, the qubit supports a native set of Clifford gates, implemented via control of the switch. The gates are topologically robust [27], and dissipatively corrected by the resistor, making them exponentially insensitive to control noise (see Fig. 8). We also find that a different encoding results in a native self-correcting T gate by a similar mechanism [28].

Achieving an efficient switched Josephson junction is a key technological challenge for the qubit. We estimate the required switch time proportional to the resonator inductance L as $\delta t_{\max} \sim 8\ \text{ps} \times L\,[\mu\text{H}]$. We thus expect the device to be feasible for L in the 5–10 μH range and switch rise times in the 40–80 ps range. This is within experimental access, with $L = 6\ \mu\text{H}$ high-impedance resonators recently realized [29], and pulse-train generators with $\lesssim 10$ ps rise times have been available for decades [30]. In Sec. IX A, we discuss possible routes to integrating such pulses with switchable Josephson junctions. Importantly, even if insufficient for DEC, an imperfect switch may still efficiently prepare and stabilize GKP states. Realizing a rapidly switchable Josephson junction may thus carry a significant reward, by enabling a self-correcting qubit with an exponentially scaling lifetime, a protected set of gates, a high operating temperature, and an intrinsic tolerance for manufacturing and control inconsistencies.

In recent years, multiple works have successfully realized GKP states in trapped-ion or circuit-QED devices through readout and feedback [19,31–33], including protocols emulating dissipation [24,34]. There have also been proposals for deterministic protocols generating GKP states through coherent driving protocols [35,36] or circuits featuring gyrators [37] and, more recently, related proposals have been proposed for dissipatively stabilizing GKP states through bath engineering via frequency combs [25] and qubit resets [34]. A key advantage of our proposal is that it realizes dissipative error correction with *generic* thermodynamic baths and a stepwise switch-activation protocol, offering a complementary approach with potentially simpler realizations. The native self-correcting single-qubit Clifford gates may also simplify the integration of the qubit in a quantum processor.

The rest of the paper is organized as follows. In Sec. II, we describe how we encode a GKP qubit in an LC resonator; in Sec. III, we introduce the self-correcting GKP qubit, discuss its basic operating principles, and demonstrate its support of topologically robust single-qubit Clifford gates. In Sec. IV, we analytically demonstrate the exponential protection of the encoded information. In Sec. V, we discuss a scheme for generating dissipatively corrected T gates in a related architecture. In Sec. VI, we discuss implementations of readout and initialization. In Sec. VII, we estimate the device criteria, operation timescales, and noise tolerances, summarized in Table I. In Sec. VIII, we provide data from numerical simulations of the device. We conclude with a discussion in Sec. IX.

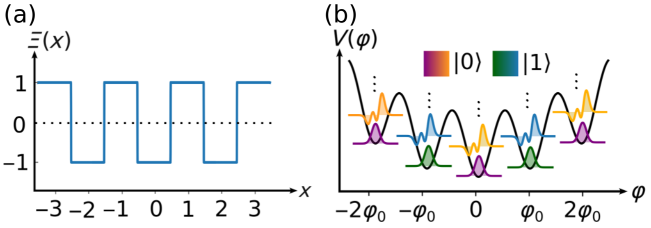

FIG. 2. GKP encoding. (a) The crenellation function Ξ used to encode the quantum information via Eq. (1). (b) Examples of logical $|0\rangle$ (purple and orange) and $|1\rangle$ (green and blue) states. The black curve indicates the flux potential from the inductor and Josephson junction (when active).

II. GKP ENCODING

The qubit is encoded in thermal ensembles of GKP states in an LC resonator [26]. In terms of the resonator flux φ and charge q, the GKP states have their Wigner-function support confined near integer multiples of φ/φ_0 and q/e, where e denotes the electron charge and $\varphi_0 = h/2e$ the flux quantum. The parities of φ/φ_0 and q/e define the σ_z and σ_x logical operators, respectively, via

$$\sigma_z = \Xi(\varphi/\varphi_0), \quad \sigma_x = \Xi(q/e), \quad \sigma_y = -i\sigma_z\sigma_x, \tag{1}$$

where $\Xi(x) \equiv \operatorname{sgn}\cos(\pi x)$ denotes the *crenellation function* (see Fig. 2), which takes value 1 when the closest integer to x is even and value -1 if the closest integer to x is odd [38,39]. Since $\Xi(x) = -\Xi(x+1)$, the above three operators satisfy the Pauli anticommutation relations

$$\{\sigma_i, \sigma_j\} = 2\delta_{ij} \tag{2}$$

and hence form a valid qubit observable. We can encode a ν-dimensional qudit in an analogous fashion (for an example, see Sec. V). The modular encoding in Eq. (1) allows *thermally mixed* physical states to encode *pure* logical states [see Fig. 2(b)]. This key feature underlies the exponential stability of our qubit.

The GKP encoding protects encoded quantum information against noise induced by finite-order polynomials of φ and q, such as charge or flux noise and photon loss—here termed *local noise*. The protection emerges because local noise generates a continuous flow of the Wigner function of the system. The logical operators $\{\sigma_i\}$ are unaffected by this flow as long as the Wigner-function support of the system does not leak across the domain boundaries located at $\varphi = (n_1 + 1/2)\varphi_0$ and $q = (n_2 + 1/2)e$ for integers n_1 and n_2. Put another way, the encoded information is protected as long as the phase-space support of the system remains confined in the span of high-eigenvalue eigenstates of the two *GKP stabilizers,*

$$S_1 = \cos\left(2\pi\varphi/\varphi_0\right), \quad S_2 = \cos(2\pi q/e). \tag{3}$$

Henceforth, we refer to the mutual high-eigenvalue subspace of S_1 and S_2 as the *code subspace* and to states within the code subspace as (generalized) GKP states.

The high degree of protection described above gives GKP codes error-correction properties on par with or superior to other bosonic encodings, such as Fock space [40], cat codes [41], and binomial codes [42]. In particular, the GKP encoding protects quantum information against any phase-space local noise and, moreover, treats phase and amplitude errors *symmetrically*. Moreover, error correction can be implemented straightforwardly through direct minimization of commuting stabilizers. Since they were first proposed [26], realizations of GKP states remained elusive for a long time. However, remarkably, recent years have seen successful realizations emerging in multiple platforms, including superconducting cavity-QED [31,34], trapped ions [19,24], and photonic chips [43].

The superconducting circuit platform we focus on is particularly suitable for GKP states, due to its intrinsic support of a powerful nonlinear element with periodicity compatible with GKP states: the Josephson junction. In this setting, GKP states can be realized as phase-coherent superpositions of states confined deep within the wells of the Josephson potential. To ensure $\langle S_2\rangle \approx 1$, the restriction of a GKP state to a single well must be approximately identical for nearby wells, up to a well-parity-dependent relative amplitude, which encodes the quantum information. The logical states of the qubit, $|0\rangle$ and $|1\rangle$, correspond to GKP states with full support in even and odd wells, respectively.

III. SELF-CORRECTING QUBIT

We now show how GKP states can be dissipatively stabilized and error corrected in the circuit device in Fig. 1(a). We also demonstrate that the device supports native protected single-qubit Clifford gates.

A. Device

The device consists of an LC resonator connected via a switch to a Josephson junction and, capacitively, to a dissipative element. Here, the dissipative element can, e.g., be a resistor or a transmission line connected to an external reservoir; for simplicity, we refer to it from here on as a resistor. The resulting circuit is described by

$$H(t) = \frac{\varphi^2}{2L} + \frac{q^2}{2C} - w_s(t)\left[E_J\cos\left(\frac{2\pi\varphi}{\varphi_0}\right) + \frac{qQ_R}{C_R}\right] + H_R, \tag{4}$$

where L and C denote the inductance and capacitance of the LC circuit and E_J is the Josephson energy of the junction, while $w_s(t)$ defines the time dependence of the switch. Additionally, H_R denotes the resistor Hamiltonian, C_R the coupler capacitance, and Q_R denotes the fluctuating charge on the resistor side of the coupler. Due to its self-correcting properties, the qubit may also operate with the resistor connected permanently to the LC resonator (for details, see Sec. VII).

B. Phase-revival trick

To see how GKP states emerge in the device, first note that activating the switch (setting $w_s = 1$) causes the system to dissipatively relax in the cosine wells from the Josephson potential, confining it in the high-eigenvalue subspace of S_1. We can stabilize S_2 by subsequently *deactivating* the switch for a quarter of the LC oscillation cycle, $\tau_{LC} \equiv 2\pi\sqrt{LC}$. In this deactivated interval, the Hamiltonian generates a $\pi/2$ rotation of phase space that interchanges φ and q up to a rescaling set by the resonator impedance, $\sqrt{L/C}$. Setting

$$\sqrt{L/C} \approx h/2e^2 \tag{5}$$

ensures that φ/φ_0 is mapped to q/e and vice versa (up to a sign), leading to an effective interchange of S_1 and S_2 [see Eq. (3)]. Hence, at the end of the deactivated segment, the distribution of charge q is confined in peaks near multiples of e, resulting in $\langle S_2\rangle \approx 1$. Reactivating the switch will again confine the system in the high-eigenvalue subspace of S_1, due to relaxation into the wells of the Josephson potential. The system will be confined in the code subspace at this point if $\langle S_2\rangle$ retains its near-unit value over the second switch-activated interval. As a key discovery, we uncover a revival mechanism that ensures that this is the case if the reactivated-switch segment has duration given by an integer multiple of the *revival time*,

$$t_{\rm rev} = \sqrt{LC}. \tag{6}$$

The revival mechanism arises because dephasing of wave-function components in distinct Josephson potential wells corresponds to diffusion of q away from multiples of e. Due to its capacitative coupling, the resistor can only generate such charge diffusion continuously and indirectly, through the inductor of the circuit. In particular, the diffusion can be slow enough to allow the peaks of the charge distribution to remain well defined and nonoverlapping on the timescale it takes for flux to relax (for details, see Sec. IV).

While wave-function components in distinct wells remain phase coherent in the presence of the *resistor*, they do acquire deterministic relative phase factors, due to their different *inductance energies*, corresponding to the vertical offset of wells in Figs. 2(b) and 4(a). In the switch-reactivated segment, these phase factors initially cause the expectation of S_2, which translates the wave function by ±2 wells, to decay to zero. However, the inductance energy for well n is given by $n^2\varepsilon_L$, where $\varepsilon_L = \varphi_0^2/2L$. Since

$$(n^2 \bmod 4) = (n \bmod 2) \quad \text{for} \quad n \in \mathbb{Z}, \tag{7}$$

wells with the same parity have inductance energies congruent modulo $4\varepsilon_L$. As a result, the phase factors from wells of the same parity *realign* at integer multiples of a *revival time* $2\pi\hbar/4\varepsilon_L = t_{\rm rev}$. At these instances, S_2 revives. This revival mechanism is clearly demonstrated in our numerical simulations—see Fig. 5(e) and shaded regions in Fig. 6(c).

The above considerations lead us to conclude that the system is stabilized in the GKP code subspace by two cycles of the switch protocol

$$w_s(t) \approx \begin{cases} 1, & 0 \quad \le t < \quad t_s, \\ 0, & t_s \quad \le t < \quad t_s + \frac{1}{4}\tau_{LC}, \end{cases} \qquad t_s = z_{\rm rev}\, t_{\rm rev}, \tag{8}$$

with $z_{\rm rev} \in \mathbb{Z}$. From here on, we refer to the $w_s = 1$ and $w_s = 0$ segments as the *stabilizer* and *free* segments, respectively.

We can also realize a ν-dimensional GKP qudit with the above scheme by setting $\sqrt{L/C} = \nu h/4e^2$ and fixing the stabilizer-segment duration to an integer multiple of $2\pi\hbar/\nu^2\varepsilon_L$. This results in the free segment generating an exchange of the stabilizers of a ν-dimensional square-lattice GKP qudit S_1 and $S_2^{(\nu)} \equiv \cos(\nu\pi q/e)$ [26] and the stabilizer segment confining the system in the high-eigenvalue subspace of S_1 while preserving the expectation value of $S_2^{(\nu)}$ via the phase-revival mechanism described above.

C. Dissipative error correction

The switch cycle in Eq. (8) is a *dissipative quantum error-correction (DEC) protocol*, in which noise-induced entropy is absorbed by the resistor, leading to protection of the encoded information (see Fig. 3): when repeated, the protocol in Eq. (8) resets any state into the code subspace every two cycles. Recall from Sec. II that local noise only generates logical errors if causing the phase-space support of the system to leak through the domain boundaries at $\varphi = (n_1 + 1/2)\varphi_0$ and $q = (n_2 + 1/2)e$ for $n_1, n_2 \in \mathbb{Z}$ [see Eq. (1)]. Logical errors can thus only occur if such leakage occurs within two cycles when starting from a stabilized state. For noise weaker than this threshold, logical error rates are exponentially suppressed. We support this claim with analytical and numerical discussions below [see Secs. IV and VIII B].

The DEC-based operating principle of the qubit contrasts to conventional quantum error correction, which utilizes a readout and feedback apparatus for removal of noise-induced entropy. This offers several advantages: first, the qubit can be stabilized without any need for

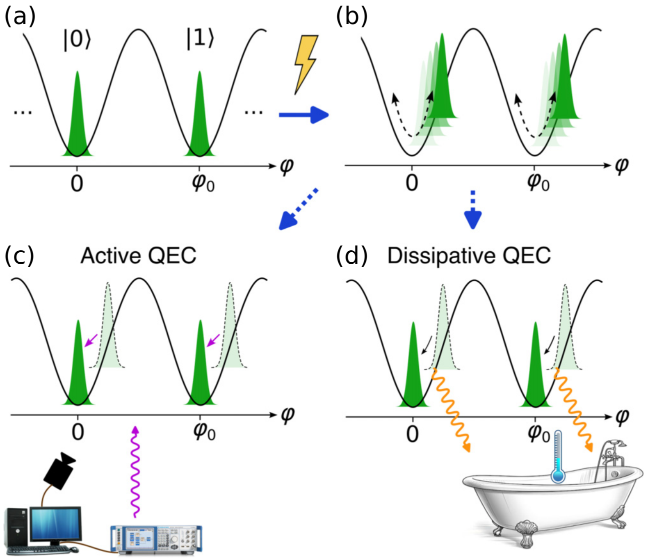

FIG. 3. An illustration of dissipative quantum error correction. (a) Quantum information is encoded in the well parity of the Josephson potential. (b) Noise excites fluctuations in the potential that will cause a bit flip via spillover between wells, if accumulating. (c) With *active quantum error correction*, a detector monitors for fluctuations and counter-steers against any with appropriate control signals, thereby absorbing noise-induced entropy analogously to Maxwell's demon. (d) With *dissipative quantum error correction*, noise-induced entropy is absorbed by thermodynamic reservoirs, via dissipative damping of fluctuations.

readout or feedback control. Additionally, DEC makes the qubit resilient to imperfections of the protocol and device, such as parameter mistargeting and control noise, since these imperfections can be viewed on par with other extrinsic noise sources and be dissipatively corrected. We estimate the finite tolerances for inconsistencies of device and driving parameters in Sec. VII (see Table I).

We finally remark that the DEC protocol protects the qubit against local noise but may fail to protect against nonlocal noise, arising from infinite-order polynomials of φ and q, which act nonlocally in phase space. Particularly relevant are quasiparticle poisoning, phase slips, and uncontrolled Cooper-pair tunneling, which translate q or φ by integer multiples of e or φ_0 and hence act nonlocally in phase space. As a result, the timescales for these processes may provide upper limits on the qubit lifetime. Mitigating these noise sources is thus crucial to achieving significant lifetime enhancement.

D. Self-correcting gates

Interestingly, the qubit natively supports protected single-qubit Clifford gates. In particular, we show how an S and Hadamard (H) gate are naturally generated by the stabilizer and free segments.

The S gate is generated through the phase-revival mechanism discussed in Sec. III B: at the zth phase revival, states in even wells have acquired a phase factor $(-i)^z$ relative to states in odd wells, since their inductance energies are congruent to 0 and ε_L modulo $4\varepsilon_L$, respectively [see Eq. (7)]. This assignment of phase factors is equivalent to z applications of the S gates, $S = e^{-i\frac{\pi}{4}\sigma_z}$. An H gate is generated by the free segment, which interchanges φ/φ_0 and q/e (up to a sign), which swaps σ_x and σ_z, equivalent to the action of a H gate. Arbitrary single-qubit Clifford control can thus be achieved via appropriate interspersing of stabilizer and free segment, e.g., by varying z_{rev}, and not necessarily ordering stabilizer and free segments in an alternating pattern.

The S and H gates are self-correcting and topologically robust [27] in the sense that the output logical state is invariant under any smooth and phase-space local perturbation of the protocol that keeps the final state within the GKP code subspace. As a result, the infidelity from control noise is *exponentially suppressed* when the noise strength below a characteristic threshold scale determined by the circuit parameters. We identify the threshold scale and estimate the exponentially suppressed error rate in Sec. VII A 2 below. In Sec. VIII C, we verify the exponential protection of the gates in simulations.

A consequence of the above results is that odd z_{rev} causes the switch protocol to cyclically permute σ_x, σ_y, and σ_z—possibly with an alternating sign. In this sense, our device can be viewed as a dissipative phase-locked oscillator, or Floquet time crystal [44–51], the emergent periodicity of which is controlled by z_{rev} mod 4. Choosing z_{rev} odd causes the three logical operators of the qubit to appear on an equal footing, implying that phase and amplitude errors are treated symmetrically and that $T_1 = T_2$. Moreover, the above symmetry means that any noise channel on the qubit is depolarizing.

IV. EXPONENTIAL SCALING OF LIFETIME

We now demonstrate the exponential scaling of the qubit lifetime in regimes in which $E_J \gg k_B T, hf_{LC}$, where T denotes the temperature of the resistor and $f_{LC} = 1/2\pi\sqrt{LC}$ the bare LC frequency. Below, we identify sufficient conditions for the emergence of a stable fixed point in the GKP code subspace, where the relaxation during the stabilizer segment only causes exponentially weak decoherence between the wells of the cosine potential from the Josephson junction. In this regime, we show that the logical error rate per protocol cycle, p_{error}, is exponentially suppressed and satisfies

$$p_{\text{error}} \lesssim \exp\left[\frac{-1}{k_B T/E_J + \pi^2\lambda_0^2}\right], \quad \lambda_0 \equiv \left(\frac{hf_{LC}}{4\pi^3 E_J}\right)^{1/4}. \tag{9}$$

Here, λ_0 denotes the vacuum fluctuation width in the cosine potential in units of φ_0 [see Fig. 4(a)] and defines a bare GKP squeezing parameter of the protocol. Here and below, $a \lesssim b$ indicates that a is bounded by b up to a subleading prefactor; in particular, $a \lesssim b$ allows a to be much smaller than b. We thus emphasize that the above bound is not necessarily tight and that the actual error rate may be exponentially smaller than the right-hand side above. When $E_J/k_B T \ll \lambda_0$, the first term in the above numerator dominates and the error rate is of order e^{-E_J/k_BT}; i.e., the error rate bound scales as an Arrhenius law. The E_J/k_BT and λ_0^2 terms can thus be viewed as the contribution of the error rate from thermal and quantum fluctuations, respectively. Importantly, we expect the exponentially scaling logical error rate to persist in the presence of device or protocol imperfections and external noise; in Sec. VII, we estimate noise tolerances based on these considerations.

The remainder of this section is devoted to establishing Eq. (9) and identifying sufficient (not necessarily required) conditions under which it holds. Technical details are provided in Appendixes A–C. The discussion is of a technical nature and readers can move directly to the more physically oriented Secs. V–IX without loss of continuity.

A. Fixed point in code subspace

We first demonstrate that the protocol has a stable fixed point in the GKP code subspace. To this end, we consider the case in which the system is initialized in the subspace of mutual eigenstates of S_1 and S_2 with eigenvalues greater than some $s_0 > -1$ and φ support confined in the range $|\varphi| \ll \varphi_0 E_J/\varepsilon_L$, where the wells of the Josephson potential remain well defined. Below, we identify *sufficient* criteria under which the protocol takes any such initial state to a fixed point at which the S_1 and S_2 support of the system remains exponentially confined near 1 [Eq. (22)].

1. Relaxation in stabilizer segment

We first consider how the state of the system $\rho(t)$ evolves in the first stabilizer segment. During this step, the circuit including the resistor is described by

$$H_s \equiv \frac{\varphi^2}{2L} + \frac{q^2}{2C} - E_J\cos\left(\frac{2\pi\varphi}{\varphi_0}\right) + \frac{qQ_R}{C_R} + H_R. \tag{10}$$

The wells of the cosine potential from the Josephson junction are approximately described as harmonic LC oscillators with capacitance C and effective inductance $L_{\text{eff}} = \varphi_0^2/4\pi^2 E_J$ [see Fig. 4(a)]. The characteristic excitation energy in the wells is given by $\varepsilon_0 \equiv \hbar/\sqrt{CL_{\text{eff}}} = \sqrt{4\pi hf_{LC}E_J}$, while the vacuum fluctuation width of φ in the wells, $\delta\varphi_0 \equiv [\hbar^2 L_{\text{eff}}/4C]^{1/4}$ is given by $\lambda_0\varphi_0$, with λ_0 defined in Eq. (9).

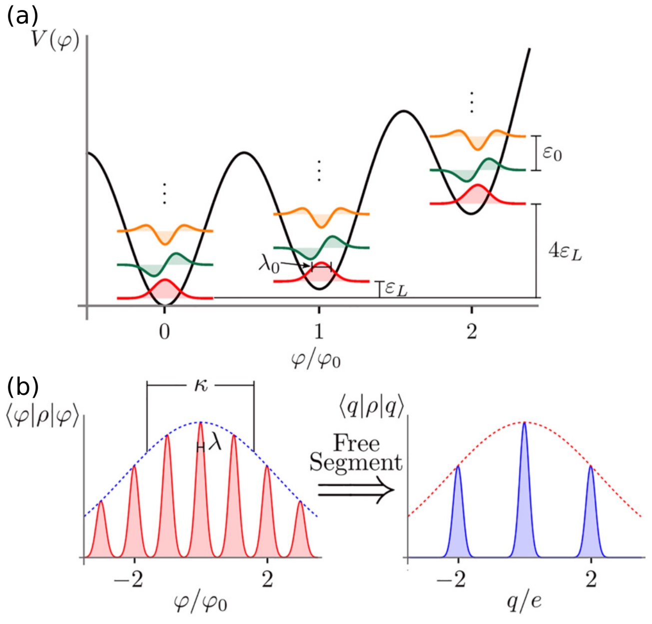

FIG. 4. Characteristic scales of the qubit. (a) Approximate low-energy eigenstates of the circuit Hamiltonian during the stabilizer segment [i.e., $w_s(t) = 1$]. To leading order in hf_{LC}/E_J, the eigenstates are harmonic oscillator eigenstates with vacuum fluctuation width $\lambda_0\varphi_0$, with $\lambda_0 = (hf_{LC}/4\pi^3 E_J)^{1/4}$, centered near $m\varphi_0$ for each $m \in \mathbb{Z}$. The corresponding excitation energy is given by $\varepsilon_0 = \sqrt{4e^2 E_J/C}$ with an overall energy shift $m^2\varepsilon_L$ in well m, where $\varepsilon_L = \varphi_0^2/2L$. (b) Left: the probability density of φ for a typical GKP state generated by our protocol (red), corresponding to a logical state $\frac{1}{\sqrt{2}}(|0\rangle + |1\rangle)$. The state is a thermal ensemble of the low-lying eigenstates of each well in (a), with thermal fluctuation width $\lambda = \lambda_0\sqrt{\coth(2\varepsilon_0/k_BT)}$, weighted by an envelope function (dashed line). Right: the result of evolving the state under the free segment. This mapping fixes the width of the envelope to be $\kappa = \sqrt{\coth(2\varepsilon_0/k_BT)}/\pi\lambda_0$ (see Appendix F).

During the stabilizer segment, the dissipation from the resistor causes the φ support of $\rho(t)$ to relax into the wells of the cosine potential from the Josephson junction. The characteristic rate for this process, Γ, can be found from the low-temperature power spectral density of the resistor $J_0(\omega) \equiv 1/2\pi \int dt e^{i\omega t}\langle Q_R(t)Q_R(0)\rangle$ via Fermi's golden rule [52–54]: $\Gamma = (\hbar C_R)^{-2} 2\pi J_0([E_{n'} - E_n]/\hbar)|\langle\psi_{n'}|q|\psi_n\rangle|^2$; here, $|\psi_n\rangle$ denotes the lowest-energy eigenstate of the nondissipative part of H_s in a given well, n, of the Josephson potential and $|\psi'_n\rangle$ denotes the eigenstate corresponding to its first excitation [see Fig. 4(a)], while E_n and $E_{n'}$ denote the corresponding energies. Noting that $E_n - E'_n \approx \varepsilon_0$, and that $|\psi_n\rangle$ and $|\psi'_n\rangle$ are adjacent Hermite functions with characteristic width $\lambda_0\varphi_0$, such that

$q|\psi_n\rangle = \hbar/\sqrt{2}\lambda_0\varphi_0|\psi_{n'}\rangle$, and using $C = e/2\pi f_{LC}\varphi_0$, the relaxation rate during the stabilizer segment is thus given by

$$\Gamma = \frac{e^2}{C_R^2\pi\hbar^2}\frac{J(\varepsilon_0/\hbar)}{\lambda_0^2}. \tag{11}$$

Since the system is already confined inside the wells of the cosine potential ($S_1 > s_0$) at the onset of the stabilizer segment, leakage of probability support between the wells is exponentially suppressed during the relaxation [55]. As a result, the flux probability distribution in well m—defined as the interval $(m-1/2)\varphi_0 < \varphi < (m+1/2)\varphi_0$—relaxes to a state approximately identical to the thermal steady state of an LC resonator with excitation energy ε_0 and vacuum fluctuation width $\delta\varphi_0$, up to a prefactor accounting for the near-conserved total probability support within each well. The thermal flux distribution of an LC resonator is given by a Gaussian with characteristic width $\delta\varphi = \lambda\varphi_0/\sqrt{2}$, where

$$\lambda = \lambda_0\sqrt{\coth(2\varepsilon_0/k_BT)}. \tag{12}$$

This dimensionless number can be viewed as a *thermally renormalized* GKP squeezing parameter and serves as the small parameter in our analysis below.

The above results imply that after the characteristic relaxation time $1/\Gamma$, the flux distribution of the system, $p_\varphi(x,t) \equiv \mathrm{Tr}[\rho(t)\delta(\varphi - x)]$, is given by

$$p_\varphi(x,t) \approx \sum_m \frac{p_m(t)}{\sqrt{2\pi}\lambda\varphi_0} e^{-\frac{(x-m\varphi_0)^2}{\lambda^2\varphi_0^2}}, \tag{13}$$

where $p_m(t) = \int_{[m-1/2]\varphi_0}^{[m+1/2]\varphi_0} dx p_\varphi(x,t)$ denotes the near-conserved steady-state probability support in well m [for an illustration, see the left panel of Fig. 4(b)]. Specifically, the leakage of probability support between the wells of the cosine potential is of order $(\varepsilon_0/h)e^{-2E_J/k_BT}$ [55], implying that the $p_m(t)$ are constants of motion in the steady state, up to $\mathcal{O}(e^{-2E_J/k_BT})$ corrections.

2. Preservation of interwell coherence

We now demonstrate that phase coherence is maintained between different wells of the cosine potential during the stabilizer segment. To account for the deterministic phase-revival mechanism described in Sec. III B, we first transform to a comoving frame generated by the unitary transformation

$$V(t) \equiv e^{-i\,\mathrm{round}(\varphi/\varphi_0)^2\varepsilon_L t/\hbar}, \tag{14}$$

where round(x) gives the integer closest to x. Evidently, $V^\dagger(t)$ assigns a phase factor $e^{im^2\varepsilon_L t/\hbar}$ to states in well m, thus canceling the phase factor from the offset of inductance energies described in Sec. III B. Reflecting the revival mechanism described there, the density matrix of the system in the rotating frame, $V^\dagger(t)\rho(t)V(t)$, coincides with that in the laboratory frame, $\rho(t)$, at multiples of the revival time $t_{\mathrm{rev}} \equiv 2\pi\hbar/4\varepsilon_L$, up to applications of a number of S gates. To see this, note that for $n \in \mathbb{Z}$, $V(nt_{\mathrm{rev}}) = e^{-i\frac{\pi}{2}n\mathrm{round}(\varphi/\varphi_0)^2}$. Using Eq. (7) and $\mathrm{round}^2(x) \bmod 4 = \frac{1}{2}(1 - \Xi(x))$, we find $V(nt_{\mathrm{rev}}) = e^{-i\frac{\pi}{4}n[1-\Xi(\varphi/\varphi_0)]}$. Recognizing $\Xi(\varphi/\varphi_0)$ as σ_z [Eq. (1)], we thus obtain

$$V(nt_{\mathrm{rev}}) = e^{\frac{-i\pi}{4}n(1-\sigma_z)} \quad \text{for} \quad n \in \mathbb{Z}. \tag{15}$$

Since $e^{-i\frac{\pi}{4}\sigma_z}$ defines the logical S gate operator, we see that $V(t_{\mathrm{rev}})$ generates an $S^\dagger$ gate and a global phase. Since $[S_2, \sigma_z] = 0$, the probability distributions for S_2 in the laboratory $[\rho(t)]$ and comoving $[V^\dagger(t)\rho(t)V(t)]$ frames coincide at integer multiples of the revival time t_{rev}.

We now show that $V^\dagger(t)\rho(t)V(t)$ remains in the high-eigenvalue subspace of S_2 during the entire stabilizer segment. To this end, we first consider the Hamiltonian in the comoving frame $H_{\mathrm{rf}}(t) = V^\dagger(t)[H_s + i\hbar\partial_t]V(t)$ [56]. We now introduce the *quasiflux* operator,

$$\bar{\varphi} \equiv \varphi \mod \varphi_0, \tag{16}$$

with the branch cut chosen at $\pm\varphi_0/2$ such that $\varphi = \bar{\varphi} + \varphi_0\mathrm{round}(\varphi/\varphi_0)$. Using $\varphi = \bar{\varphi} + \varphi_0\mathrm{round}(\varphi/\varphi_0)$, a straightforward calculation yields $H_{\mathrm{rf}}(t) = \tilde{H} + \Delta H_{\mathrm{rf}}(t)$ with

$$\tilde{H} = \tilde{H}_0 + \mathrm{round}\left(\frac{\varphi}{\varphi_0}\right)\frac{\varphi_0\bar{\varphi}}{L}, \tag{17}$$

$\Delta H_{\mathrm{rf}} = -iV^\dagger\left[q^2/2C - qQ_B/C_R, V\right]$ and

$$\tilde{H}_0 = \frac{\bar{\varphi}^2}{2L} - \frac{q^2}{2C} - E_J\cos\left(\frac{2\pi\bar{\varphi}}{\varphi_0}\right) + \frac{qQ_R}{C_R} + H_R. \tag{18}$$

Importantly, $[\bar{\varphi}, S_2] = 0$ [57], implying $[\tilde{H}_0, S_2] = 0$.

We now show that ΔH_{rf} can be neglected: recall that $V(t)$ assigns a piecewise-constant phase factor to eigenstates of φ. Since $q = -i\hbar\partial_\varphi$, the φ support of ΔH_{rf} is thus confined to infinitesimally small neighborhoods surrounding $\varphi = (z + 1/2)\varphi_0$ for each $z \in \mathbb{Z}$. Since the support of the system in this region is of order e^{-2E_J/k_BT} [55], ΔH_{rf} can thus be neglected at the cost of an exponentially suppressed correction. Indeed, in Appendix A, we show that the time evolution generated by $\tilde{H}$, $\tilde{\rho}(t) \equiv e^{-i\tilde{H}t}\rho(0)e^{i\tilde{H}t}$ remains exponentially close to $V^\dagger\rho V$ at all times, $\|V^\dagger(t)\rho(t)V(t) - \tilde{\rho}(t)\|_{\mathrm{tr}} \lesssim \mathcal{O}(e^{-E_J/k_{\mathrm{B}}T})$, with $\|\cdot\|_{\mathrm{tr}}$ denoting the trace norm.

Having neglected $\Delta H_{\mathrm{rf}}(t)$, we consider the evolution of S_2 in the comoving frame, $\langle\tilde{S}_2\rangle \equiv \mathrm{Tr}[\tilde{\rho}S_2]$. Recalling that $[S_2,\bar{H}]=0$ and $\partial_t\tilde{\rho}=-i/\hbar[\tilde{H},\tilde{\rho}]$, explicit calculation shows that $\partial_t\langle\tilde{S}_2\rangle=-\mathrm{Tr}\,[(2\bar{\varphi}\varphi_0/\hbar L)\sin(2\pi q/e)\tilde{\rho}]$. Using that $|\mathrm{Tr}[\rho A]|\leq\sqrt{\mathrm{Tr}[A^\dagger A\rho]}$ for any density matrix ρ and that $\sin^2(x)\leq 1$, this implies that

$$|\partial_t\langle\tilde{S}_2\rangle|\leq\frac{2\pi}{\varphi_0 t_{\mathrm{rev}}}\sqrt{\langle\bar{\varphi}^2\rangle},\tag{19}$$

where we have used $t_{\mathrm{rev}}=\pi\hbar L/\varphi_0^2$. From this result, we conclude two things. First, since $\langle\bar{\varphi}^2\rangle\leq\varphi_0^2/4$, $|\partial_t\langle\tilde{S}_2\rangle|\leq\pi/t_{\mathrm{rev}}$ at all times. Second, after the relaxation, for the quasithermal steady state in Eq. (13), where $\langle\bar{\varphi}^2\rangle=\lambda\varphi_0$, $|\partial_t\langle\tilde{S}_2\rangle|\leq 2\pi\lambda/t_{\mathrm{rev}}$. Thus $\langle\tilde{S}_2\rangle$ should remain near constant on the revival timescale t_{rev}, provided that $\lambda\ll 1$.

In Appendix B, we extend the above result to demonstrate that not only the expectation value but the entire *probability support* of S_2 can remain near stationary in the comoving frame over a revival time when $\lambda\ll 1$. Specifically, for any $k>0$, the cumulative probability support for S_2, $\mathcal{P}_2(s,t)\equiv\mathrm{Tr}[\theta(s-S_2)\tilde{\rho}(t)]$ satisfies

$$\mathcal{P}_2(s,t)\lesssim e^{-k[s_0-s-\Delta s_k(t)]},\tag{20}$$

where $\Delta s_k(t)\equiv-\int_0^t d\tau\, v_k(\tau)$ and

$$v_k(t)\equiv\frac{\mathrm{Tr}[\tilde{\rho}_k(t)\bar{\varphi}\sin\frac{2\pi q}{e}]}{\varphi_0 t_{\mathrm{rev}}/2\pi},\quad\tilde{\rho}_k\equiv\frac{e^{\frac{-kS_2}{2}}\tilde{\rho}(t)e^{\frac{-kS_2}{2}}}{\mathrm{Tr}\left[e^{-kS_2}\tilde{\rho}(t)\right]}.\tag{21}$$

For each k, $v_k(t)$ defines a maximal velocity for the spread of S_2 support, beyond which it must decrease exponentially at rate k. Hence, it defines a speed limit for interwell dephasing, akin to the Lieb-Robinson velocity. In the regime $k\gg 1$, the S_2 support of $\tilde{\rho}(t)$ must be confined above $s_2-\Delta s_k(t)$. In this sense, interwell coherence is maintained as long as $\Delta s_k(t)<1-s_0$ for large k.

We now show that $\Delta s_k(t)$ remains much smaller than 1 during the entire stabilizer segment when

$$\lambda\ll 1\quad\text{and}\quad\Gamma t_{\mathrm{rev}}\ll 1.\tag{22}$$

To this end, we consider the $\bar{\varphi}$-support range of $\rho(t)$, $\Delta\varphi(t)$ [58]. The evolution is unaffected if, at time t, we restrict the system to the subspace with $|\bar{\varphi}|\leq\Delta\varphi(t)$ [59]. Next, we use that $|\mathrm{Tr}[X\rho]|\leq\|X\|$ for any density matrix ρ, where $\|X\|$ is the singular-value norm of X. Using that the above truncation leads to $\|\bar{\varphi}\sin(2\pi q/e)\|\leq\Delta\varphi(t)$ at time t and noting that $\tilde{\rho}_k(t)$ is a density matrix, we find from Eq. (21) that

$$v_k(t)\leq\frac{2\pi}{t_{\mathrm{rev}}}\frac{\Delta\varphi(t)}{\varphi_0}.\tag{23}$$

We now note that $\Delta\varphi(t)$ is trivially bounded by $\varphi_0/2$. Moreover, during the stabilizer segment, $\Delta\varphi(t)$ should relax to approximately $2\pi\lambda\varphi_0$ on the characteristic relaxation timescale $1/\Gamma$ [60]. Thus, $v_k(t)$ is bounded by a number that relaxes from at most π/t_{rev} to $2\pi\lambda/t_{\mathrm{rev}}$ on the timescale $1/\Gamma$, implying $\Delta s_k(t)\lesssim\pi/\Gamma t_{\mathrm{rev}}+2\pi\lambda(t)/t_{\mathrm{rev}}$. Evidently, $\Delta s_k(t)$ remains much smaller than 1 on the timescale t_{rev} if the conditions in Eq. (22) are satisfied. We again emphasize that these are sufficient, but not necessarily required, conditions for preservation of phase coherence during the stabilizer segment. In particular, phase coherence may remain preserved even when $\Gamma t_{\mathrm{rev}}\lesssim 1$.

3. Fixed point

We now demonstrate that a stable fixed point emerges in the code subspace under the conditions in Eq. (22).

We first consider the evolution of the cumulative probability distribution for S_1, $\mathcal{P}_1(s,t)\equiv\mathrm{Tr}[\theta(s-S_1)\tilde{\rho}(t)]$; note that $V(t)$ commutes with S_1, implying that the distributions for S_1 are identical in the laboratory (ρ) and comoving ($\tilde{\rho}$) frames. Due to the Gaussian confinement of φ near integer multiples of φ_0 [Eq. (13)], the cumulative probability distribution for S_1, $\mathcal{P}_1(s,t)\equiv\mathrm{Tr}[\theta(s-S_1)\tilde{\rho}(t)]$, is given by approximately $\mathrm{erfc}(\arccos(s)/2\pi\lambda)$ at the end of each stabilizer segment. Using $\mathrm{erfc}(x)\sim e^{-x^2}$ and $\arccos(s)\sim\sqrt{2-2s}$, we can rewrite this as

$$\mathcal{P}_1(s,t)\lesssim\exp\left[\frac{s-1}{2\pi^2\lambda^2}\right].\tag{24}$$

This result holds for $t\gg 1/\Gamma$.

We next note that the free segment interchanges S_2 and S_1. Hence, at the onset of the second and all subsequent stabilizer segments, $\mathcal{P}_2(s,t)$ equals the right-hand side of Eq. (24), implying that the S_2 support of the system is initially exponentially confined near 1 in the regime $\lambda\ll 1$. Moreover, under the conditions in Eq. (22), the probability support for S_2 is effectively constant during stabilizer segment. As a result, we find that

$$\mathcal{P}_2(s,t)\lesssim\exp\left[\frac{s-1}{2\pi^2\lambda^2}\right]\tag{25}$$

in the second, and all subsequent, stabilizer segments; this result is obtained systematically in Appendix B.

Finally, we again recall that the free segment interchanges the probability distributions for S_1 and S_2; we conclude that at the onset of the third and all subsequent stabilizer segments, $\mathcal{P}_1(s,t)\lesssim\exp\left[(s-1)/2\pi^2\lambda^2\right]$. Noting that this is consistent with the steady-state flux distribution in the stabilizer segment [Eq. (13)], we anticipate little change of this distribution during the stabilizer segment and hence we expect that Eq. (24) remains satisfied throughout the this and all subsequent stabilizer segments. As a result, we conclude that two cycles of the driving protocol take the system to a fixed point satisfying Eqs. (24) and (25).

B. Exponential scaling of lifetime

We finally demonstrate the exponential suppression of the logical error rate quoted in Eq. (9).

First note that the density matrix in the comoving frame, $\tilde{\rho}$, remains exponentially confined in the code subspace during the stabilizer segment [Eqs. (24) and (25)]. From the considerations in Sec. II, this should imply that the expectation values of the logical operators in the state $\tilde{\rho}(t)$ remain exponentially invariant during the stabilizer segment. In Appendix C, we confirm this intuition via explicit computation, showing that, for $i = 1, 2, 3$, and throughout the stabilizer segment

$$|\mathrm{Tr}[\sigma_i \tilde{\rho}(t)] - \mathrm{Tr}[\sigma_i \tilde{\rho}(0)]| \lesssim \exp\left[\frac{-1}{k_B T/E_J + \pi^2 \lambda_0^2}\right]. \tag{26}$$

Here, we have suppressed power-law prefactors on the right-hand side; for expressions involving these, see Appendix C. We now recall that $V^\dagger(t)\rho(t)V(t)$ differs from $\tilde{\rho}(t)$ by a $\mathcal{O}(e^{-E_J/k_BT})$ correction and that $V(t_s)$ is identical to the z_{rev}th power of the logical S gate operator. Hence, the expectation values of the logical operators at the end of the stabilizer segment ($t = t_s$) relate to those at the onset ($t = 0$) through

$$\langle \boldsymbol{\sigma}(t_s)\rangle = \mathcal{S}^{z_{\mathrm{rev}}}\langle \boldsymbol{\sigma}(0)\rangle + \delta\boldsymbol{\sigma}_{\mathrm{error}}, \tag{27}$$

where $\mathcal{S}$ denotes the 3×3 Bloch-sphere rotation matrix corresponding to an S gate [61] and

$$|\delta\boldsymbol{\sigma}_{\mathrm{error}}| \lesssim \exp\left[-\frac{1}{k_B T/E_J + 4\pi \lambda_0^2}\right]. \tag{28}$$

Here, we have suppressed prefactors on the right-hand side, which scale as a power law with λ_0^{-1} and E_J/k_BT and thus are subdominant in the limit $\lambda_0^{-1}, E_J/k_BT \gg 1$. Identifying $p_{\mathrm{error}} = |\delta\boldsymbol{\sigma}_{\mathrm{error}}|$ leads to Eq. (9).

V. PROTECTED *T* GATE WITH ALTERNATIVE ENCODING

Here, we show how a protected T gate can be realized using an alternative configuration of the qubit, based on an alternative encoding scheme and a resonator with impedance $\sqrt{L/C} = h/e^2$ [28]. The T gate can be realized using the quasimodular logical operators $\bar{\boldsymbol{\sigma}} = (\bar{\sigma}_x, \bar{\sigma}_y, \bar{\sigma}_z)$, where

$$\bar{\sigma}_z = \Xi(\varphi/\varphi_0), \quad \bar{\sigma}_x = e^{-i\frac{q}{2e}} I I_{\mathrm{m}}, \quad \bar{\sigma}_y = -i\bar{\sigma}_z\bar{\sigma}_x. \tag{29}$$

Here, $\Xi(x)$ denotes the crenellation function, while I and I_{m} denote the phase space and *modular* inversion operators, respectively: letting $|\phi\rangle$ denote the φ eigenstate with eigenvalue ϕ, these are defined by $I|\varphi\rangle = |-\varphi\rangle$ and $I_{\mathrm{m}}|z\varphi_0 + \delta\varphi\rangle = I_{\mathrm{m}}|z\varphi_0 - \delta\varphi\rangle$ for $|\delta\varphi| \le \varphi_0/2$ and $z \in \mathbb{Z}$. The above logical operators satisfy $\{\bar{\sigma}_i, \bar{\sigma}_j\} = \delta_{ij}$ and hence form a valid qubit observable [62].

With the above encoding, the code subspace is spanned by 4 families of states, with support near $\varphi \bmod 4\varphi_0 = \zeta\varphi_0$ for $\zeta = 0, 1, 2$, or 3, respectively. The computational spaces split up into two sectors: logical operators do not couple states with $\zeta \in \{0, 1\}$ to states with $\zeta \in \{2, 3\}$. We use the first sector as the computational space for the system, with $\zeta = 0, 1$ resulting in eigenvalues 1 and -1 of $\bar{\sigma}_z$. States with $\zeta = 2, 3$ can be considered noncomputational. The logical operators $\{\bar{\sigma}_i\}$ have stabilizers S_1 and $\bar{S}_2 = \cos(4\pi q/e)$. The above quasimodular encoding can thus be dissipatively stabilized by the device and protocol in Sec. III B by setting $\sqrt{L/C} = h/e^2$. The revival of $\bar{S}_2$ in the stabilizer segment is again ensured by picking the stabilizer-segment duration to be an integer multiple of $\tau_{LC}/2\pi$: to see this, note that the inductance energy is given by $\varepsilon_L = \pi h f_{LC}/4$, implying that states in well m acquire a relative phase factor $e^{-iz_{\mathrm{rev}}\pi m^2/4}$ after the stabilizer segment. Since $(n+4)^2 - n^2 \in 8\mathbb{Z}$, revival of $\bar{S}_2$ is ensured for each integer choice of z_{rev}.

The T gate emerges because the $|\zeta\rangle$ logical state (for $\zeta \in \{0, 1\}$) has support in wells where $m \bmod 4 = \zeta$. Since $m \bmod 4 = \zeta$ implies $m^2 \bmod 8 = \zeta$ for $\zeta \in \{0, 1\}$, the $|\zeta\rangle$ logical state of the qubit acquires a phase factor $e^{-i\pi\zeta/4}$ during the stabilizer segment. A stabilizer segment with $z_{\mathrm{rev}} \in 8\mathbb{Z} + 1$ hence generates a T gate [63].

Unlike the modular encoding in Eq. (1), the above quasimodular encoding does not appear to support a native protected Hadamard gate and hence also not universal gates. The T protocol could be used as a high-fidelity magic factory that generates magic states on the physical-qubit level with exponentially suppressed infidelity.

VI. READOUT AND INITIALIZATION

We now describe a possible way to measure σ_z via the supercurrent in the Josephson junction. The protocol can also be used for initialization in a logical $|X\rangle$ state (i.e., a state with $\langle\sigma_x\rangle = 1$). The protocol consists of the following sequence:

(1) Activate the switch ($w_s = 1$) for a duration $\tau_{LC}/4\pi$.
(2) Deactivate the switch ($w_s = 0$) for a duration $\tau_{LC}/4$.
(3) Reactivate the switch and measure the squared supercurrent in the Josephson junction, $I^2 = (2eE_J/\hbar)^2 \sin^2(2\pi\varphi/\varphi_0)$, e.g., from the frequency shift of an adjacent transmon due to the induced magnetic field [64,65]. In this interval, the relaxation time Γ^{-1} (controlled through C_R) must be longer than the detection time of the device.
(4) If the average squared supercurrent is larger than $I_c^2/4$, the system was in a $|1\rangle$ logical state

($\langle\sigma_x\rangle = -1$) at the onset of the readout protocol. If not, the system was in a $|0\rangle$ logical state at the onset.

(5) (*For initialization*): deactivate the switch again after a duration $z_{\rm readout}/(2\pi f_{LC})$, where $z_{\rm readout}$ is an integer large enough to ensure successful measurement of the supercurrent. If no supercurrent is detected, the system is initialized in a logical state with $\langle\sigma_x\rangle = 1$ at the end of the protocol. If a supercurrent *is* detected, run the ordinary stabilization protocol for a few cycles and repeat the above steps.

The readout protocol exploits a characteristic peak structure that emerges in the charge support of GKP states during the stabilizer segment, $p_q(x) \equiv {\rm Tr}[\delta(q-x)\rho]$. At times $t = a\tau_{LC}/(2\pi b)$ for $a, b \in \mathbb{Z}$, the charge support of ρ is confined near multiples of $q = e/b$. Furthermore, if b is even, the parity of the multiple reveals σ_z: a logical $|s\rangle$ state, with σ_z eigenvalue $(-1)^s$, will have charge support confined near $(2n+s)e/b$ for $n \in \mathbb{Z}$. The peak structure is evident in Figs. 5(a) and 5(d), where we plot the evolution of $p(q)$ during the stabilizer segment starting from two different logical states with σ_z eigenvalue -1 [Fig. 5(a)] and 1 [Fig. 5(d)] [66]. The structure emerges due to a shear drift of the peaks of the Wigner function of the system, $W(\varphi, q)$ during the stabilizer segment. At time t, all peaks located at flux $\varphi = n\varphi_0$ have shifted in the q direction by an amount $2\pi n e f_{LC} t/2$. This causes distinct Wigner-function peaks to align in the φ direction for rational $2\pi f_{LC} t$, leading to emergence of peaks in the charge probability distribution, $p(q) = \int d\varphi W(\varphi, q)$, as illustrated in Figs. 5(a)–5(c). The mechanism is discussed in further detail in Appendix G.

The readout protocol exploits the peak structure as follows. Step 1 of the protocol evolves the system until a time $t = \tau_{LC}/4\pi$ ($a = 1, b = 2$), where a logical $|s\rangle$ state will have its q support confined near $(n + s/2)e$ for integer n. Step 2 maps q/e to $-\varphi/\varphi_0$, implying that the φ support of the resulting state is confined near $(n + s/2)\varphi_0$ for $n \in \mathbb{Z}$. If the system is in a $|1\rangle$ logical state, the physical state will have its φ support confined near the maxima of the Josephson potential. During step (3), the system will thus decay to the ground state of the Josephson potential, leading to a detectable supercurrent signal. On the other hand, for a $|0\rangle$ logical state, the system will be deep in the wells of the Josephson potential at the onset of step (3) and no supercurrent will be detected.

The above protocol can be used for initialization: by starting from a random initial state, a few cycles of the stabilization protocol first drives the system into the code subspace. Subsequently, the readout protocol is applied. If no supercurrent was detected, the system is known to have even support in all wells after the readout protocol, i.e., to be in a logical $|X\rangle = \frac{1}{\sqrt{2}}(|0\rangle + |1\rangle)$ state. If a nonzero supercurrent is detected, the system is in an undetermined state (since the relaxation into the wells will cause the measured $|1\rangle$ state to be destroyed and replaced by a mixed logical state). In that case, the stabilization and readout protocol is repeated until no supercurrent is detected.

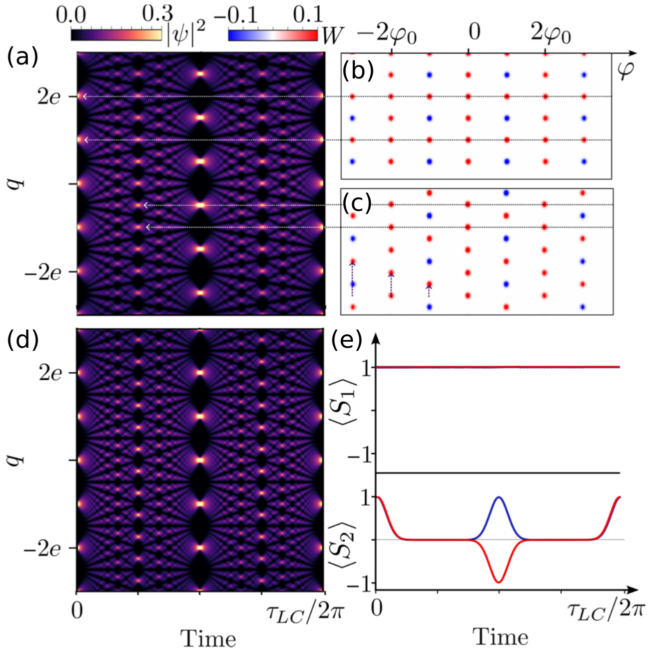

FIG. 5. The evolution of logical states during the stabilizer segment. The data are obtained with parameters $E_J/h = 200$ GHz and $f_{LC} = 0.82$ GHz, in the absence of the resistor and charge noise. (a) The evolution of the charge support $p(q)$ during the stabilizer segment for a logical $|1\rangle$ state. (b),(c) The Wigner function of the system at (b) $t = 0$ and (c) $t = \tau_{LC}/(8\pi)$. The horizontal arrows indicate correspondence to peaks in (a) and the purple arrows indicate shear drift of peaks in the Wigner function. (d) The evolution of the charge probability distribution for a logical $|0\rangle$ state. (e) The evolution of stabilizers during the stabilizer segment for the $|0\rangle$ (red) and $|1\rangle$ state (blue).

Importantly, noise from the readout apparatus does not affect the stability of the qubit during its normal operation. Specifically, the squared supercurrent $I^2 = (2eE_J/\hbar)^2 \sin^2(2\pi\varphi/\varphi_0)$ commutes with the logical operators $\{\sigma_i\}$; noise coupled to it hence cannot decohere the encoded information. Indeed, the supercurrent readout can work as a syndrome detector, if switched on during the normal operation of the qubit.

VII. NOISE TOLERANCE, DEVICE REQUIREMENTS, AND TIMESCALES

Here, we characterize the performance of the qubit in the presence of device and control imperfections or noise and estimate the parameter requirements for the qubit. We also estimate relevant operational timescales. We list our estimated device requirements, noise tolerances, and

TABLE I. The operating regime and operation timescales for three parameter scenarios. Estimates are obtained in Sec. VII, for an error tolerance of $p_{\text{error}} = 0.0003$ per cycle (four standard deviations). Parameters L, C, E_J, Γ, and z_{rev} denote the inductance, capacitance, Josephson energy, resistor-induced loss rate, and stabilizer-segment duration in units of the revival time $t_{\text{rev}} \equiv \sqrt{LC}$, respectively. f_{LC} and λ_0 denote the derived LC frequency and GKP squeezing parameters. The charge- and flux-noise thresholds denote the estimate maximal tolerated power spectral density for a white-noise charge or flux signal. For noise tolerances and device requirements below the listed thresholds, we expect the qubit lifetime to remain exponentially long. The parameters in columns 1 and 2 are within experimental access, with $L = 6$ μH, $C \approx 23$ fF resonators achieved in Ref. [29] and pulse train generators available with rise times below 10 ps [30].

Parameters			
L (μH)	2.5	6	10
C (fF)	15	40	60
E_J/h (GHz)	200	65	200
Γ (GHz)	2	1	0.5
z_{rev}	8	4	8
f_{LC} (GHz)	0.82	0.32	0.21
λ_0	0.08	0.08	0.05
Device requirements			
Switch rise time (ps)	16	43	45
LC quality factor	520	1400	2000
Maximum temperature (K)	0.58	0.16	0.9
Accuracy of L/C (%)	8	9	6
Noise thresholds			
Charge noise (e^2/Hz)	4×10^{-12}	1×10^{-11}	2×10^{-11}
Flux noise (φ_0^2/Hz)	3×10^{-12}	5×10^{-12}	5×10^{-12}
Operation timescales			
Protocol cycle (ns)	2	3	7
H gate (ns)	0.3	0.8	1.2
S gate (ns)	0.2	0.5	0.8
Readout (ns)	75	75	75
Initialization (ns)	310	310	320

operational timescales for three different parameter scenarios in Table I; each requirement and threshold is estimated for a tolerated logical error probability per cycle $p_{\text{error}} \approx 0.0003$ corresponding to four standard deviations (see below for details). We estimate the error probability based on the displacement or deformation of phase space effectively induced by the error sources we consider. In this analysis, we make use of a dimenionless measure of phase-space displacement, defined as $\Delta s = \sqrt{(\Delta\varphi/\varphi_0)^2 + (\Delta q/e)^2}$ for a given displacement in phase space $(\Delta\varphi, \Delta q)$.

A. Device requirements

We first estimate the device requirements, focusing on the Josephson energy, impedance, temperature, control resolution, and quality factor of the LC resonator.

1. Josephson energy and temperature

We estimate the minimal required Josephson energy using the error-bound estimate in Eq. (9),

$$p_{\text{error}} \lesssim \exp\left(-\frac{-1}{k_{\text{B}}T/E_J + \pi^2\lambda_0^2}\right),$$

where $\lambda_0 = \left(hf_{LC}/4\pi^3 E_J\right)^{1/4}$. The error rate $p_{\text{error}} \sim 0.0003$ hence requires $(k_{\text{B}}T/E_J) + \pi^2\lambda_0^2 \lesssim 1/8$, leading to the following estimate for the minimal required Josephson energy and maximal temperature:

$$E_J \gtrsim 60hf_{LC}, \quad k_BT \lesssim E_J/8 - \sqrt{E_J hf_{LC}}. \tag{30}$$

We emphasize that the above thresholds are obtained from the error estimate in Eq. (9), which may be a relatively loose upper bound. The qubit may thus operate at Josephson energies smaller than, and temperatures larger than, the thresholds that we identify above.

2. Switch rise time

We next estimate the condition on the switch rise time. A finite rise time Δt causes the free segment to effectively mistarget the $\pi/2$ rotation of phase space by an angle $\delta\theta$, where $\delta\theta \sim 2\pi f_{LC}\Delta t/2$. We estimate the induced error rate to be given by the total phase support experiencing a phase-space displacement greater than 1/2 by this additional rotation (in terms of the dimensionless phase-space displacement measure introduced in the beginning of this section). In Appendix F, we show that the Wigner-function envelope of the system is a Gaussian with standard deviation $\kappa/\sqrt{2}$ in these units, where $\kappa = \sqrt{\coth(2\varepsilon_0/k_BT)}/\pi\lambda_0$ and $\varepsilon_0 = \sqrt{4\pi E_J hf_{LC}}$ (see also Fig. 4). This leads us to estimate p_{error} as the probability weight of this Gaussian envelope beyond distance $1/2\delta\theta$. Using $1/2\delta\theta \sim 1/2\pi f_{LC}\Delta t$ and working in the limit of low temperatures, where $\kappa \approx 1/\pi\lambda_0$, leads to

$$p_{\text{error}}(\Delta t) \sim e^{-\frac{\lambda_0{}^2}{4f_{LC}^2\Delta t^2}}. \tag{31}$$

For comparison, we have plotted this estimate together with numerically obtained error rates in Fig. 8. For a logical error rate corresponding to $p_{\text{error}} = 0.0003$, which requires $E_J \gtrsim 60$, such that $\lambda_0 \sim 0.1$, we hence estimate a minimal rise time of order $\Delta t_{\max} \sim 0.02/f_{LC}$. We emphasize that the switch must be completely turned off in the bulk of the free segment to ensure preservation of logical information. If this is not the case, spurious tunneling of Cooper pairs may induce irrecoverable logical errors. We thus expect the qubit to only be resilient to switch mistiming, with imperfect switch deactivation causing logical errors (though still allowing generation of GKP states—see Sec. IX A).

3. Impedance

Next, we consider the tolerance for mistargeting the impedance, $Z = \sqrt{L/C}$. A finite deviation of impedance $\delta Z \equiv Z - h/2e^2$ leads to a squeezing of the Wigner function over a free segment by the factor $2\delta Ze^2/h$. Analogously to our condition for control resolution, we estimate the error rate to be given by the phase-space support of the system in the region in which the squeezing-induced displacement exceeds 1/2. Recalling that the Wigner function of the system has a Gaussian envelope of width $\kappa \sim 1/\pi\lambda_0$, this leads to

$$p_{\text{error}}(\delta Z) \sim e^{-\frac{\pi^2 {\lambda_0}^2}{4[2e^2\delta Z/h]^2}}. \tag{32}$$

With $p_{\text{error}} = 0.0003$ and $\lambda_0 \sim 0.1$ (as required to reach this error rate), this leads to a window of approximately 700Ω (i.e., approximately 5% tolerance for relative deviations). Because of the square root, the tolerance for relative deviations of L and C is twice that of Z, up to approximately 10%.

4. Quality factor

We next consider the consequences of a finite Q factor of the LC resonator caused by uncontrolled capacitative coupling to its surrounding environment—i.e., photon loss. During the stabilizer segment, a capacitative coupling to an external environment is beneficial; indeed, such a coupling is leveraged by our dissipative stabilization protocol. During the free segment, the capacitive coupling, on the other hand, results in a uniform loss rate of photons from the LC resonator, at the rate $\gamma = 2\pi f_{LC}/Q$, where Q is the corresponding quality factor [53]. Working in units where $\varphi_0 = e = 1$, photon loss generates simultaneous uniform diffusion and shrinkage of phase space, with diffusion constant $\gamma \coth(hf_{LC}/2k_BT)$ and shrinkage rate γ [67]. At the end of the free segment, after a duration $1/4f_{LC}$, photon loss has thus shrunk phase space by a factor of approximately $(1-\gamma/4f_{LC})$ and diffused it with a diffusion kernel of standard deviation $\Delta = \sqrt{\gamma \coth(hf_{LC}/2k_BT)/4f_{LC}}$. We estimate the logical error rate as the phase-space weight experiencing a displacement greater than 1/2 by the diffusion kernel or the total phase-space weight experiencing a displacement greater than 1/2 by the phase-space shrinkage, whichever is largest. Recalling that the envelope of the Wigner function is a Gaussian with standard deviation $\kappa/\sqrt{2}$, this leads to the estimate $p_{\text{error}} \sim \max\{\exp(-1/8\Delta^2), \exp(-4f_{LC}^2/\kappa^2\gamma^2)\}$. Using the expression for Δ along with $Q = 2\pi/\gamma\tau_{LC}$,

$$p_{\text{error}}(Q) \sim \max\left\{ e^{-\frac{Q}{4\pi}\tanh\frac{hf_{LC}}{2k_\text{B}T}},\ e^{-\lambda_0^2 Q^2} \right\}. \tag{33}$$

Working in the regime $f_{LC} \sim 1$ GHz, $T \sim 100$ mK and for $p_{\text{error}} \sim 0.0003$ (requiring $\lambda_0 \gtrsim 0.1$), this leads to the condition $Q_{\min} \sim 450$. This relatively mild condition raises the possibility that the dissipative element can permanently connected to the resonator, possibly in combination with appropriate filtering of bath modes.

B. Tolerance for noise

Here, we analyze the effects of flux and charge noise.

1. Charge noise

We model charge noise as a fluctuating charge $\xi(t)$ capacitively coupled to the circuit through $H_q(t) = \xi(t)q/C$. For simplicity, we assume that $\xi(t)$ a white-noise signal, with uniform power spectral density $\gamma_q/2\pi$, such that $\langle \xi(t)\xi(t')\rangle = \gamma_q\delta(t-t')$. On its own, $H_q(t)$ generates Brownian motion of the flux, φ, with diffusion constant $D_q = \gamma_q/C^2$ [53]. Within the stabilizer segment, dissipation from the resistor counteracts the diffusion, driving φ toward the minima of the flux potential, $\varphi = n\varphi_0$. We expect the qubit to remain stable in the stabilizer segment if the effective diffusion length within the resistor-induced relaxation time Γ^{-1} is much smaller than $\varphi_0/2$, i.e., if $D_q \ll \Gamma\varphi_0^2$. Within the free segment, $H_q(t)$ generates diffusion in phase space along the direction $(\varphi_0\cos(2\pi f_{LC}t), e\sin(2\pi f_{LC}t))$ with normalized diffusion constant $D = D_q/\varphi_0^2$ in units where $e = \varphi_0 = 1$. As a result, $H_q(t)$ generates correlated flux and charge displacements with variances both given by $\sigma_q^2 = D\tau_{LC}/8$ in the free segment. We estimate the error rate to be the phase weight experiencing a phase-space displacement greater than 1/2, $p_{\text{error}} \sim e^{-1/8\sigma_q^2}$. Using $C = e^2/\pi hf_{LC}$, this leads to [68]

$$p_{\text{error}}(\gamma_q) \sim e^{-\frac{e^2}{4\pi^2\gamma_q f_{LC}}}. \tag{34}$$

For a tolerated error rate of $p_{\text{error}} = 0.0003$ and $f_{LC} \sim 1$ GHz resonators, we thus require $\gamma_q \lesssim 3 \times 10^{-12} e^2/\text{Hz}$.

2. Flux noise

Finally, we consider flux noise, which we model as a white-noise fluctuating flux $\xi_\varphi(t)$ coupled to the system through $H_\varphi = \xi_\varphi(t)\varphi/L$, where $\langle \xi_\varphi(t)\xi_\varphi(t')\rangle = \gamma_\varphi\delta(t-t')$. On its own, this term generates random diffusion of the charge and causes a phase-space displacement during the free segment, $(\Delta\varphi, \Delta q)$. Since no mechanism counteracts charge diffusion during the stabilizer segment, flux noise also generates a charge displacement in the stabilizer segment with diffusion constant $D_\varphi = \gamma_\varphi/L^2$. This displacement is only corrected in the following cycle, where it has been mapped to a flux displacement. Over this duration, the flux-noise induced diffusion kernel has acquired a variance $\sigma_\varphi^2 = D_\varphi\tau_{LC}/8 + D_\varphi t_s/2$ along the charge quadrature and a variance $\sigma_\varphi^2 = D_\varphi\varphi_0^2\tau_{LC}/8e^2$ along the flux quadrature. Combining the diffusion during the stabilizer and free segments, an analysis similar to the one performed for charge noise results in the error rate estimate

$$p_{\rm error}(\gamma_\varphi) \sim e^{-\frac{\varphi_0^2}{\pi^2[4+z_{\rm rev}/2\pi]\gamma_\varphi f_{LC}}}. \tag{35}$$

Using $z_{\rm rev} \sim 1$, $p_{\rm error} \sim 0.0003$, and $f_{LC} \sim 1\,\text{GHz}$, we obtain the requirement $\gamma_\varphi \lesssim 3 \times 10^{-12}\varphi_0^2/\text{Hz}$.

C. Operation timescales

We estimate the readout and initialization times using the native protocol described in Sec. VI, assuming that the squared supercurrent of the Josephson junction can be detected within approximately 75 ns with a Josephson-device based magnetometer [64,65]. The detection time is estimated assuming that the magnetometer is located 5 µm from the Josephson junction and has a sensitivity of approximately 10 $\text{pT}/\sqrt{\text{Hz}}$, as has been realized recently [64,65]. The initialization time is estimated assuming a 50% probability for successful initialization at each attempt (see Sec. VI), implying that an average of four attempts are required to initialize the qubit.

The gate times are estimated using the native gates of the qubit, described in Sec. III D: the S gate $e^{-i\pi\sigma_z/4}$ is generated by a stabilizer segment with duration $1/(2\pi f_{LC})$, while the Hadamard gate is generated by a free segment, with duration $1/(4 f_{LC})$ (for further discussion of the gates, see Sec. III D).

VIII. NUMERICAL RESULTS

We now verify our analytical results given above with numerical simulations of the qubit.

To demonstrate the self-correcting properties of the qubit, we include charge noise throughout the simulations, modeling the system via the master equation

$$\partial_t \rho = \Big(\mathcal{L}_s(t) + \mathcal{L}_{\rm noise}(t)\Big)[\rho], \tag{36}$$

where $\mathcal{L}_s(t)$ and $\mathcal{L}_{\rm noise}(t)$ are the time-evolution generators (Liouvillians) of the stabilization protocol and charge noise, respectively. We use the universal Lindblad equation (ULE) to model the dissipative dynamics in the stabilizer segment [54,69–73], via

$$\mathcal{L}_s(t)[\rho] = -\frac{i}{\hbar}[H_{\rm S}(t),\rho] + w_s(t)\left[\ell\rho\ell - \frac{1}{2}\{\ell^\dagger\ell,\rho\}\right], \tag{37}$$

where $H_{\rm S}(t) = q^2/2C + \varphi^2/2L - w_s(t)E_J\cos(2\pi\varphi/\varphi_0)$ denotes the nondissipative component of the system Hamiltonian and

$$\ell \equiv \frac{1}{\hbar C_R}\sum_{mn}|\psi_m\rangle\langle\psi_n|\sqrt{2\pi J([E_n-E_m]/\hbar)}\langle\psi_m|q|\psi_n\rangle \tag{38}$$

denotes the ULE jump operator for the system with the switch activated. Here, $|\psi_n\rangle$ and E_n denote the energies and eigenstates of the Hamiltonian for the circuit formed by the inductor, capacitor and Josephson junction, $H_{\rm LCJ} \equiv q^2/2C + \varphi^2/2L - E_J\cos(2\pi\varphi/\varphi_0)$ and $J(\omega)$ the power spectral density of the resistor. We model the resistor as an Ohmic bath at temperature T, such that $J(\omega) = g^2\omega(1-e^{-\hbar\omega/k_{\rm B}T})^{-1}$, for some constant g [52–54], which fixes the loss rate at $\Gamma = 4(ge/C_R\hbar)^2E_J/\hbar$ [see Eq. (11) [74]]. The ULE is rigorously proven to be valid in the regime of weak loss rate relative to the intrinsic correlation timescales of the bath (the latter of order h/k_BT for Ohmic baths) [54,73]. Capturing both relaxation and interwell decoherence, we thus expect this model to provide an accurate representation of the dynamics.

We model charge noise through the Liouvillian

$$\mathcal{L}_{\rm noise}[\rho] = -i\frac{\xi_q(t)}{\hbar C}[q,\rho], \tag{39}$$

where $\xi_q(t)$ is a scalar white-noise field satisfying $\langle\xi(t)\xi(t')\rangle = \gamma_q\delta(t-t')$, with γ_q defining the charge-noise strength. We set $\gamma_q = 10^{-12}\,e^2/\text{Hz}$ throughout the simulations, unless otherwise noted. We expect the white-noise model to accurately capture effects of generic charge noise. In particular, we expect that low-frequency noise, such as $1/f$ noise, is also phase-space local (and hence efficiently correctible by our protocol) and will have similar effects on the system: its high-frequency components are qualitatively similar to the white-noise signal that we consider, while low-frequency components can be viewed as slow modulation of device parameters, against which the protocol is also resilient.

We numerically solve Eq. (36) for various parameter sets, using the stochastic Schrodinger equation (SSE) [75,76], and with ℓ computed through exact diagonalization. Being agnostic to the analysis in Secs. III–IV, our simulation thus serves as an independent check of its conclusions.

A. Stabilization of GKP states

To verify that the protocol stabilizes GKP states, we have initialized the system in a random high-energy state far outside the code subspace [77] and computed the resulting evolution under the protocol via the SSE, for parameters $E_J/h = 200$ GHz, $L = 2.5$ µH, $C = 15$ fF, $z_{\rm rev} = 2$, and $T = 200$ mK. In Fig. 6(a), we show the evolution of the flux probability density for a representative

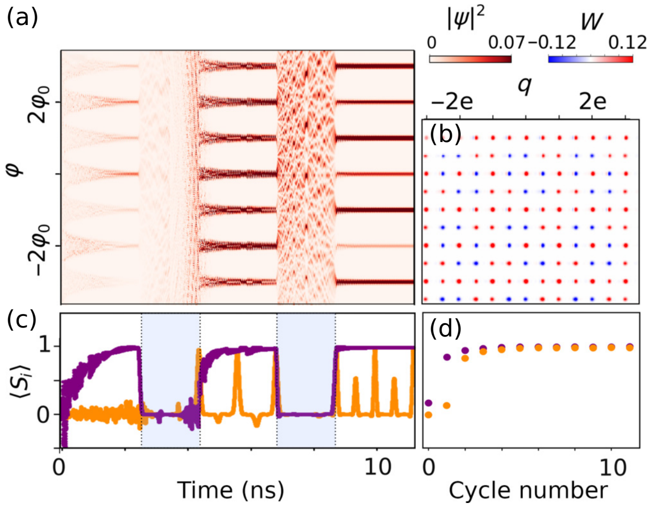

FIG. 6. Dissipation-driven convergence to the GKP code subspace (for details, see Sec. VIII A). (a) The simulated evolution of the flux probability distribution over three cycles obtained for a single stochastic-Schrodinger-equation (SSE) trajectory and starting from a random initial state [77], using $E_J/h = 200$ GHz, $L = 2.5$ μH, $C = 15$ fF, $z_{\mathrm{rev}} = 2$, and $T = 200$ mK. (b),(c) The (b) Wigner function of the final state and the (c) evolution of stabilizers 1 (purple) and 2 (orange) for the trajectory depicted in (a). The shaded regions indicate stabilizer segments. Note that $\langle S_2 \rangle$ is only required to take a value near 1 at the end of each stabilizer segment for the GKP states to be stabilized. (d) The mean value of the stabilizers at the end of each stabilizer segment for the first 12 cycles, averaged over 100 trajectories.

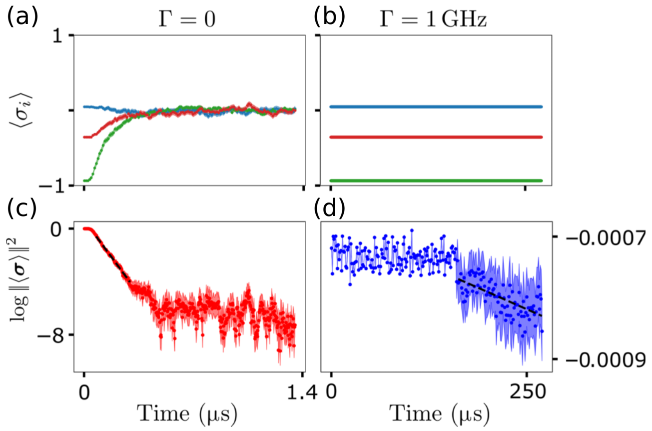

FIG. 7. A demonstration of dissipative quantum error correction. We use parameters $E_J/h = 200\,\mathrm{GHz}$, $L = 10$ μH, $C = 60$ fF, $z_{\mathrm{rev}} = 8$, and $T = 40$ mK. (a),(b) The simulated evolution of logical operators in the (a) absence and (b) presence of coupling to the resistor, averaged over 200 SSE trajectories, starting from a randomly chosen logical state (see the text). (c),(d) The logarithm of the logical Bloch-vector length, $\log\|\boldsymbol{\sigma}\|^2$, versus time, in the (c) absence and (d) presence of coupling to the resistor—note the different x- and y-axis scales in the panels. The dashed lines indicate fits used to estimate qubit lifetimes. The data in (d) are obtained by time coarse-graining evolution of $\|\boldsymbol{\sigma}\|^2$ over 400 driving periods before taking the logarithm. The shaded regions, where visible, indicate the standard error of the mean in (a) and (b) and the standard deviation from bootstrap resampling of SSE trajectories in (c) and (d).

SSE trajectory from this simulation. The single trajectory approaches the center of the wells of the Josephson potential (integer multiples of φ_0) in each stabilizer segment, while retaining support in different wells—reflecting the maintenance of interwell coherence, consistent with our discussion in Sec. IV. After three cycles, the Wigner function of the trajectory has the characteristic GKP grid structure [Fig. 6(b)], indicating successful convergence to the code subspace. Indeed, the expectations of the two stabilizers have relaxed to near unity after two cycles [Fig. 6(c)]. Sampling over 100 SSE trajectories, we confirm that stabilization of GKP states is achieved within two or three cycles of the protocol (approximately 8 ns) [Fig. 6(d)].

B. Dissipative error correction

To confirm that the logical information is dissipatively error corrected by the protocol, we compute the evolution of the system for many subsequent cycles, after initializing the system in a randomly selected computational state [78]. In Fig. 7, we show the resulting evolution of logical operators for $\Gamma = 0$ and $\Gamma = 1$ GHz, averaged over 200 trajectories and using parameters $E_J/h = 200$ GHz, $L = 10$ μH, $C = 60$ fF, $z_{\mathrm{rev}} = 8$, and $T = 40$ mK. Whereas the logical-operator expectations quickly decay in the absence of the resistor, for $\Gamma = 1$ GHz, the logical operators remain stationary over the entire window that we simulate.

To further illustrate the DEC of the qubit, in Fig. 1(d) we show the stabilizers and logical-operator evolution for representative SSE trajectories at 3 values of Γ. Evidently, increasing Γ causes the fluctuations of the stabilizers away from unity to decrease and the logical operator trajectories to become stationary, implying the stabilization of the encoded information. Note that the logical operators for $\Gamma = 1\,\mathrm{GHz}$ remain stationary in the presence of significant thermal fluctuations of the stabilizers, and hence also the state. This demonstrates that the encoded information is successfully decoupled from the thermal noise from the resistor. Interestingly, it is also possible to distinguish individual logical error events for $\Gamma = 0.25$ GHz in Fig. 1(d): here, the stabilizers only reach negative values in a few instances, where rare (but significant) noise-induced fluctuations take the system over the energy barrier that protects the qubit. Indeed, the logical operator remains near stationary between these instances but changes abruptly at instances where the stabilizers obtain negative values. We estimate the qubit lifetime via the decay of the logical state Bloch-vector length, $\|\langle \boldsymbol{\sigma} \rangle\|^2$. In Fig. 7(c), we show the stroboscopic evolution of $\log\|\langle \boldsymbol{\sigma} \rangle\|^2$ for $\Gamma = 0$. The

Bloch-vector length remains near unity for a brief initial period of little decay, which we expect is due to the finite time required for the phase-space support of the system to reach the domain boundaries of the logical operators. Beyond this point, the data show a clear linear trend consistent with exponential decay of the Bloch-vector length. From a linear fit [dashed line in Fig. 7(c)], we estimate a lifetime of 63^{+19}_{-9} ns, with errors indicating the 95% confidence interval from bootstrap resampling of SSE trajectories. In Fig. 7(d), we show the evolution of $\log\|\langle\boldsymbol{\sigma}\rangle\|^2$ for $\Gamma = 1$GHz [note the different x and y scales compared to Fig. 7(c)] [79]. The logarithm of the Bloch-vector length exhibits a clear linear decrease after an initial period of approximately 150 μs where the information is near stationary [80]. From a linear fit of the data after the onset of exponential decay [dashed line in Fig. 7(d)] [81], we estimate a lifetime of $1.8^{+9.9}_{-1.1}$ s (where the errors are the 95% confidence interval from bootstrap resampling). While there is significant uncertainty in our estimate of the lifetime, it is clear that the presence of the resistor enhances the timescales over which quantum information is preserved up to macroscopic timescales.

To investigate the scaling of the qubit lifetime with the dissipation strength, in Fig. 1(b) we show the evolution of the obtained coherence times as a function of Γ, for the device parameters from column three of Table I. The data reveal an exponential trend that continues beyond the 1-ms range for $\Gamma \gtrsim 0.6$ GHz, indicating a potential for significant qubit stability against phase-space local noise.

C. Robustness of gates against switch mistiming

We next investigate the resilience of the qubit to switch mistiming, Δt. Such mistiming qualitatively captures the effects of both imperfect control as well as the finite rise time of the switched Josephson junction. This analysis also serves as a check of the gate infidelity for the native S and H gates of the qubit (recall that these gates—or a power thereof—are generated by each stabilizer and free segment, respectively.

To analyze the effects of finite Δt, for each cycle of the protocol we have randomly changed the duration of each stabilizer and free segment by δt and $-\delta t$ respectively, preserving the total cycle duration; we have made this choice to reflect that the period of the signal is precisely controllable by available electronics. For each cycle, δt is drawn uniformly on the interval $[-\Delta t/2, \Delta t/2]$, with Δt as a parameter that we vary. We expect that this randomly mistimed protocol also captures the dynamics of a smooth ramp of a realistic switch at a qualitative level.

In Fig. 8, we plot the error rate per S gate (stabilizer segment) and H gate (free segment), as a function of Δt, using parameters $E_J/h = 200$ GHz, $L = 2.5$ μH, $C = 15$ fF, $\Gamma = 2$ GHz, and $T = 40$ mK. We also include an analytical estimate based on Eq. (31), combined with the baseline level from Eq. (9), $p(\Delta t) = e^{-\lambda_0{}^2/4\pi f_{LC}^2 \Delta t^2} + p_0$, where $p_0 = e^{-1/4\pi\lambda_0{}^2}$ is the estimated upper bound on the error rate per cycle in the absence of any protocol imperfections. Note that p_0 dominates for $\Delta t \leq 12$ ps. Evidently, the error rate exhibits a clear exponential dependence on Δt, which follows the analytical estimate reasonably well down to p_0, beyond which the exponential decrease continues down to a rate consistent with the exponential lifetime enhancement observed in Fig. 1(b), significantly undershooting p_0. This possibly reflects that p_0 is a loose upper bound on the error rate, as discussed in Sec. IV. We also note that the error per gate remains around approximately 10^{-6} for mistiming $\Delta t \sim 10$ ps. Given the availability of pulse train generators with rise times below 10 ps [30], this suggests that our device may be within reach of current experimental capabilities, provided that one can control the Josephson Junction on these timescales (which we discuss in the next section).

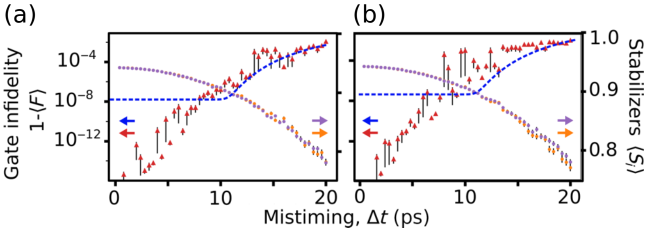

FIG. 8. The exponential suppression of the gate infidelity. We use parameters $E_J/h = 200$ GHz, $L = 2.5$ μH, $C = 15$ fF, $\Gamma = 2$ GHz, and $T = 40$ mK. The gate infidelity (red; left axis) and steady-state values of the GKP stabilizers (purple and orange; right axis) for the native (a) S and (b) H gates of the protocol, as a function of switch mistiming. The blue dashed lines indicate the analytically estimated error-rate bound from Eq. (31) (for more details, see the text). All data points shown are averaged over 10^3 SSE trajectories.

D. Readout

Finally, we have simulated the readout protocol from Sec. VI, using parameters $E_J/h = 200$ GHz, $L = 10$ μH, $C = 60$ fF, $T = 40$ mK, and $z_{\text{rev}} = 8$. We have first generated characteristic $|0\rangle$ and $|1\rangle$ logical states of the protocol by evolving initial states with support in only even and only odd wells of the cosine potential, respectively, for 18 cycles. We have then simulated the evolution of the system during the readout protocol from Sec. VI. During step (3) of the protocol, we have decreased the effective resistor conductance to $ge/C_R\hbar = 0.00016$, in order to extend the relaxation time of the supercurrent signal to the approximately 100-ns range, where it can possibly be detected (see Sec. VI). In the simulation, we have used the charge-noise strength $\gamma_q = 0.1 \times 10^{-13}\, e^2$/Hz, because the smaller value of $\kappa e/C_R\hbar$ leads to a lower tolerance for charge noise.

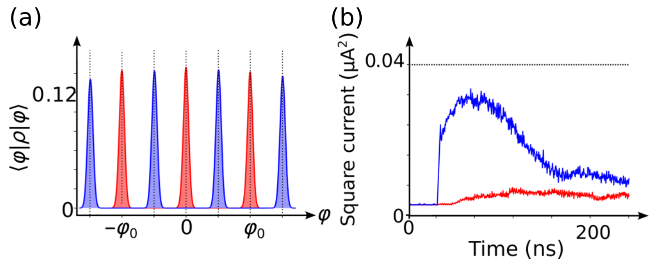

FIG. 9. Numerical simulations of the readout protocol (see Sec. VI). We use parameters $E_J/h = 200$ GHz, $L = 10$ μH, $C = 60$ fF, and $T = 40$ mK. (a) The flux probability density, $\langle\varphi|\rho|\varphi\rangle$, at the onset of step (3) of the protocol, immediately before the measurement of the squared supercurrent. Here, the system is initially in a logical state produced by the protocol with σ_z expectation 1 (red) and −1 (blue). (b) The evolution of the squared supercurrent during step (3) of the protocol (supercurrent measurement), for the two initializations.

In Fig. 9(a), we show the flux probability density, $\langle\phi|\rho|\phi\rangle$, at the onset of step (3) of the protocol, for the two different initializations, averaged over 50 SSE trajectories. As described in Sec. VI, the distributions resulting from the two logical states are confined near integer and half-integer multiples of φ_0, respectively. In Fig. 9(b), we show the evolution of the squared supercurrent during step (3), $\langle I^2\rangle = (2eE_J/h)^2 \sin^2(2\pi\varphi/\varphi_0)$, with $t = 0$ denoting the onset of the readout protocol. Evidently, the two different logical states result in very different supercurrent signals, which could be detected by a readout device.

IX. DISCUSSION AND CONCLUSION

In this work, we have proposed a circuit-QED architecture for a dissipatively error-corrected GKP qubit. Our analytical and numerical results indicate that the self-correcting property of the qubit gives rise to an exponentially scaling lifetime, even in the presence of extrinsic noise or device and control imperfections. DEC leads to exponential lifetime increase. We have moreover demonstrated that the qubit supports a set of native, rapidly operated, and self-correcting single-qubit Clifford gates, the infidelity of which we expect will be exponentially suppressed. Also enhancing its appeal, the qubit supports a native readout and initialization protocol via the Josephson-junction supercurrent. If similar protocols can be identified for multiqubit and magic gates, our results raise the possibility of a self-correcting quantum information processor.

A. Experimental considerations

The key technological challenges that we foresee for our proposal are the realization of a resonator with impedance 12.91 kΩ, along with a controllable Josephson junction with a rapid rise time Δt. For a given tolerated error rate per cycle, $p_{\rm error}$, the maximal rise time Δt is determined from Eq. (40). For instance, with a tolerated error rate of $p_{\rm error} = 0.0003$ (four standard deviations), which requires setting E_J large enough that $\lambda_0 \lesssim 0.1$ [through Eq. (9), we require $\Delta t \lesssim 0.02/f_{LC}$. Using $f_{LC} = h/4\pi e^2 L$, the condition on the rise time for a four-standard-deviation error tolerance thus becomes

$$\Delta t_{\rm max} \approx 8\,{\rm ps} \times L\,[\mu{\rm H}]. \tag{40}$$

We expect this to be a reasonable estimate for the practically required rise time of the qubit. Note that the estimate is in agreement with our simulations (Fig. 8). Recently, high-impedance resonators have been achieved with $L = 6\,\mu$H and $> 12.9\,$kΩ [29], leading to a required rise time of order 50 ps; for other recent realizations of high-impedance resonators, see also Refs. [82–84]. In such a configuration, we estimate that the gate times of the qubit can be of order $0.5 - 1$ ns, while the readout and initialization times can be of order 75 ns and 300 ns, respectively (see Sec. VII). This condition on the rise time can be relaxed further if the current progress proceeds beyond 6 μH inductances.

An approximately 50-ps rise time is, in principle, compatible with existing technology: pulse-train generators exist with rise times below 10 ps [30], while Josephson junctions have been demonstrated to operate with control frequencies in the 70-GHz range without succumbing to losses from quasiparticles and other sources [85]. The main experimental challenge that we anticipate for our proposal, then, is to integrate the pulse to a fast-rise-time Josephson coupler. Such an integration could, e.g., be realized with high-mobility semiconductor-based Josephson junctions controlled by gate electrodes [86,87]. An alternative approach is superconducting quantum interference device (SQUID) junctions controlled by flux lines [35,88], where 10-GHz high-fidelity flux control has been demonstrated [89–91]. A third option is the voltage biasing of one or more junction terminals [92]. It is also possible that a combination of the above approaches can be used to achieve the required switch time and high on-off ratio.

Our results show that the self-correcting GKP qubit is exponentially robust against phase-space local noise. At the same time, its lifetime may be limited by phase-space-*nonlocal* noise, including residual effective Josephson energy of the junction in the free segment due to imperfect deactivation. Any spurious Cooper-pair tunneling during due to imperfect deactivation may directly induce noncorrectable logical errors by generating nonlocal displacements in phase space. We thus anticipate a hierarchy of independent success criteria for the suppression rate of the switch:

(a) Suppressing E_J well below hf_{LC} will likely lead to dissipative *generation of GKP states*, since the oscillator evolution in this case will be dominated by free phase-space rotation in the free segment.

(b) Suppressing E_J by many orders of magnitude below hf_{LC} may, moreover, lead to significant lifetime enhancement from *dissipative error correction*, due to spurious Cooper-pair tunneling being effectively absent over a large number of cycles.

In addition to incomplete deactivation of the Josephson junction, we expect quasiparticles to be an important phase-space nonlocal noise source that could limit the qubit lifetime. Quasiparticle-poisoning events may effectively translate q by up to e, constituting a phase-space nonlocal process that can potentially cause noncorrectable logical errors [93]. At the same time, we expect this noise source to only matter when quasiparticles are accumulated in the capacitor, i.e., when the charge fluctuation created by the quasiparticle has significant and persistent mutual capacitance with the resonator mode encoding the qubit. Hence, quasiparticle trapping [94] and device engineering may offer routes to preventing quasiparticle poisoning from adversely affecting the qubit. Moreover, experiments report that poisoning rates in the $\mathrm{m\,s^{-1}}$ range can be reached [95,96], suggesting that quasiparticle-induced errors can be rare enough to be efficiently mitigated by active quantum error correction.

B. Outlook

Our results suggest that the architecture proposed here will result in a qubit that is autonomously error corrected on the physical-qubit level, with a lifetime that scales exponentially, up to limits set by quasiparticle events and the inverse residual Josephson energy of the junction in the deactivated mode. The qubit can, moreover, operate at temperatures approximately in the 0.1–1 K range and does not require pristine resonators (we estimate the required quality factor down to the 200–1000 range; see Table I) or perfect control over the driving signal or the device parameters. Finally, the qubit supports rapid single-qubit Clifford gates with exponentially suppressed gate infidelity. These features could significantly simplify the integration of the qubit into a quantum information processor and facilitate active error-correction schemes based on the device.

DEC on the physical-qubit level also raises the important possibility of parallel control of many qubits. Specifically, the self-correcting properties of the qubit give it an intrinsic tolerance for deviation of device parameters and control signals. In particular, varying response to a global control signal arising from device-to-device deviations would be corrected by the native stabilization protocol, provided that the device-parameter errors are within the thresholds that we have identified in Sec. VII. The ability to manufacture and control large numbers of qubits in parallel is a key component to scalable quantum computation and so far has proved a challenge in superconducting circuits. Our device offers the exciting possibility of achieving this lofty goal.

Due to the above advantages, we expect the qubit proposed here to offer a promising alternative route to scalable quantum computation, bypassing key scalability challenges for approaches purely based on active error correction.

An interesting future direction is to explore whether the device supports a universal set of native self-correcting gates, by exploring realizations of self-correcting multiqubit and non-Clifford gates, along with the integration of the qubit into a quantum information processor that supports efficient universal gate and readout protocols. It is particularly interesting that our platform supports a self-correcting native magic (T) gate with the quasimodular encoding described in Sec. V. We speculate that this mechanism can be leveraged as a resource for protected magic gate generation—i.e., a magic factory—in a future quantum information processing architecture [28].

ACKNOWLEDGMENTS

We gratefully acknowledge useful discussions with Philippe Campagne-Ibarcq, Max Geier, Lev-Arcady Sellem, Jacob Hastrup, Luca Banzerus, Karsten Flensberg, Jonathan Conrad, and Dolev Bluvstein. F.N. was supported by the U.S. Department of Energy, Office of Science, Basic Energy Sciences under Award No. DE-SC0019166, the Simons Foundation under Award No. 623768, the Carlsberg Foundation, under Grant No. CF22-0727 and by the Novo Nordisk Foundation, Grant No. NNF22SA0081175, NNF Quantum Computing Programme. G.R. is grateful for support from the Simons Foundation as well as from the National Science Foundation (NSF) Division of Materials Research (DMR) under Grant No. 1839271, and from the Institute for Quantum Information and Matter (IQIM), an NSF Physics Frontiers Center. L.J. acknowledges support from the Army Research Office (ARO) (Grant No. W911NF-23-1-0077), the ARO Multidisciplinary University Research Initiative (MURI) (Grant No. W911NF-21-1-0325), the Air Force Office of Scientific Research (AFOSR) MURI (Grants No. FA9550-19-1-0399, No. FA9550-21-1-0209, and No. FA9550-23-1-0338), the Defense Advanced Research Projects Agency (DARPA) (Grants No. HR0011-24-9-0359 and No. HR0011-24-9-0361), the National Science Foundation (Grants No. OMA-1936118, No. ERC-1941583, No. OMA-2137642, No. OSI-2326767, and No. CCF-2312755), and the Packard Foundation (Grants No. 2020-71479). This work was performed in part at the Aspen Center for Physics, which is supported by NSF Grant No. PHY-1607611. The computations presented here were, in part, conducted in the Resnick High Performance Computing

Center, a facility supported by Resnick Sustainability Institute at the California Institute of Technology.

DATA AVAILABILITY

The data in this study are not publicly available. The data are available from the authors upon reasonable request.

APPENDIX A: EFFECTIVE HAMILTONIAN IN COMOVING FRAME

Here, we demonstrate that the Hamiltonian $\tilde{H}$ describes the evolution in the comoving frame introduced in Sec. IV, up to an exponentially suppressed correction to the state of the system. To recap, we consider the time evolution in the comoving frame, reached through the transformation

$$V(t) = e^{-i\varepsilon_L M^2 t}, \quad \text{where} \quad M \equiv \text{round}(\varphi/\varphi_0). \tag{A1}$$

We refer to M as the *well index operator* throughout this and the following appendixes. Our goal is to show that, throughout each stabilizer segment, the density matrix of the system, $\rho_{\rm rf}(t) \equiv V^\dagger(t)\rho(t)V(t)$, is exponentially close to the time evolution generated by $\tilde{H}$ [given in Eq. (17)], $\tilde{\rho} \equiv e^{-i\tilde{H}t}\rho_0 e^{i\tilde{H}t}$. Specifically, we will show that

$$\|\rho_{\rm rf} - \tilde{\rho}\|_{\rm tr} \lesssim e^{-\frac{E_J}{k_B T}}, \tag{A2}$$

where $\|\cdot\|_{\rm tr}$ denotes the trace norm, $\|A\|_{\rm tr} = \text{Tr}[\sqrt{A^\dagger A}]$.

To establish the above results, we exploit that M is an integral of motion of the dynamics of $\rho(t)$ in the laboratory and comoving frames, up to corrections of order $e^{-2\frac{E_J}{k_B T}}$ [55]. More precisely, we show in Appendix D that when the system is confined in a finite φ range at the onset of the stabilizer segment, $-w_0\varphi_0 \leq \varphi \leq w_0\varphi_0$ with $w_0 \ll E_J/hf_{LC}$, then, for any functions f and g,

$$\|[U, f(M)]g(M)\rho_0\|_{\rm tr} \lesssim \sqrt{\frac{\varepsilon_0 t}{\hbar}}\, e^{-\frac{E_J}{k_B T}} w_0 \|g\| \|f\|, \tag{A3}$$

where $\|g\| = \max_{|w| \leq w_0} |g(w)|$ and $U \equiv e^{-iH_s t}$ denotes the evolution operator of the full system in the laboratory frame throughout the stabilizer segment. Here and below, the notation $x \lesssim y$ indicates that x is smaller than or equal to y, up to an $\mathcal{O}(1)$ prefactor; in particular, $x \lesssim y$ allows x to be much smaller than y. The initial confinement $|\varphi| \leq \varphi_0 w_0$ is assumed for the initialization (see the beginning of Sec. IV) and remains justified during subsequent protocol cycles, where the flux probability distribution has a Gaussian envelope of width $\kappa\varphi_0$, where $\kappa = \sqrt{\coth(2\varepsilon_0/k_{\rm B}T)}/\pi\lambda_0$ (see Appendix F), implying that we can set $w_0 \sim \kappa$ after the first protocol cycle [97]. In particular, recall that $\lambda_0^{-1} \sim (E_J/hf_{LC})^{1/4}$, while we require $E_J \gg hf_{LC}$, such that $(E_J/hf_{LC})^{1/4}$, and hence also κ is much smaller than E_J/hf_{LC}.

As a key intermedicate step in establishing Eq. (A2), we introduce the *ancillary* density matrix ρ_a, defined by assigning the phase factor $e^{-i\varepsilon_L t/\hbar m^2}$ to states in well m *before* time evolving:

$$\rho_a \equiv UV^\dagger \rho_0 V U^\dagger. \tag{A4}$$

Below, we will show that ρ_a is close to both $\rho_{\rm rf}$ and $\tilde{\rho}$, thereby establishing Eq. (A2) via the triangle inequality.

To bound the distance between $\rho_{\rm rf}$ and ρ_a, we note that, by definition,

$$\rho_{\rm rf} \equiv V^\dagger U \rho_0 U^\dagger V. \tag{A5}$$

Since spillover of probability support between wells during the time evolution with U is exponentially suppressed, it makes little difference whether we assign the well-dependent phase factor (through the unitary V) *before* or *after* time evolving, implying that $\rho_{\rm rf} \approx \rho_a$. Specifically, note that $\rho_{\rm rf} - \rho_a = [U, V^\dagger]\rho_0 V U^\dagger + V^\dagger U \rho_0 [V, U^\dagger]$, implying that $\|\rho_{\rm rf} - \rho_a\|_{\rm tr} \leq 2\|[U, V^\dagger]\rho_0\|_{\rm tr}$ [98]. Note that $\|[U, V^\dagger]\rho_0\|_{\rm tr}$ is of the form on the left-hand side of Eq. (A3) with $f(x) = e^{-ix^2\varepsilon_L t/\hbar}$ and $g(x) = 1$. Hence, we find

$$\|\rho_a - \rho_{\rm rf}\|_{\rm tr} \lesssim w_0 \sqrt{\frac{\varepsilon_0 t}{\hbar}}\, e^{-\frac{E_J}{k_B T}}. \tag{A6}$$

To bound the distance from ρ_a to $\tilde{\rho}$, we take the time derivative in Eq. (A4). Using $\partial_t U = -iH_s U$, we obtain

$$\partial_t \rho_a = -\frac{i}{\hbar}[H_s, \rho_a] + \frac{i}{\hbar}\varepsilon_L[UM^2U^\dagger, \rho_a]. \tag{A7}$$

We next note that $UM^2U^\dagger\rho_a = UM^2V^\dagger\rho_0 VU^\dagger$, implying that

$$UM^2U^\dagger\rho_a - M^2\rho_a = [U, M^2]V^\dagger\rho_0 VU^\dagger. \tag{A8}$$

We use Eq. (A3) to bound the trace norm of the second term above, with $f(x) = x^2$, implying that $\|f\| = w_0^2$, and $g(x) = e^{-ix^2\varepsilon_L t/\hbar}$, implying that $\|g\| = 1$. Doing this, we obtain

$$\|[U, M^2]V^\dagger\rho_0 VU^\dagger\|_{\rm tr} \lesssim w_0^3 \sqrt{\frac{\varepsilon_0 t}{\hbar}}\, e^{-\frac{E_J}{k_B T}}. \tag{A9}$$

Combining Eqs. (A8) and (A9), we find that

$$\|[UM^2U^\dagger, \rho_a] - [M^2, \rho_a]\|_{\rm tr} \lesssim w_0^3 \sqrt{\frac{\varepsilon_0 t}{\hbar}}\, e^{-\frac{E_J}{k_B T}}. \tag{A10}$$

Using this result in Eq. (A7), we arrive at

$$\partial_t \rho_a = -\frac{i}{\hbar}[H_s - M^2\varepsilon_L, \rho_a] + \delta\dot{\rho}_a, \tag{A11}$$

where

$$\|\delta\dot{\rho}_a\|_{\rm tr} \lesssim \frac{\varepsilon_L}{\hbar}\sqrt{\frac{\kappa^3\varepsilon_0 t}{\hbar}}e^{-\frac{E_J}{k_B T}}.$$

Comparing with Eq. (17), we recognize $H_s - M^2\varepsilon_L = \tilde{H}$—this follows when using $\varphi = \bar{\varphi} + M\varphi_0$. Thus,

$$\partial_t \rho_a = -\frac{i}{\hbar}[\tilde{H}, \rho_a] + \delta\dot{\rho}_a. \tag{A12}$$

Finally, we use the above result to bound the distance between ρ_a and $\tilde{\rho} \equiv e^{-i\tilde{H}t}\rho_0 e^{i\tilde{H}t}$. Using $\rho_a(0) = \rho_0$, integrating Eq. (A12) results in

$$\rho_a(t) = e^{-i\tilde{H}t}\rho_0 e^{i\tilde{H}t} + \int_0^t ds e^{-i\tilde{H}(t-s)}\delta\dot{\rho}_a(s)e^{i\tilde{H}(t-s)}, \tag{A13}$$

where we have restored the explicit time dependence. Recognizing the first term on the right-hand side above as $\tilde{\rho}(t)$, we thus find that

$$\|\rho_a(t) - \tilde{\rho}(t)\|_{\rm tr} \leq \int_0^t ds \|\delta\dot{\rho}_a(s)\|_{\rm tr}. \tag{A14}$$

Next, we use

$$\|\delta\dot{\rho}\|_{\rm tr} \lesssim \frac{\varepsilon_L}{\hbar}w_0^3\sqrt{\frac{\varepsilon_0 t}{\hbar}}e^{-\frac{E_J}{k_B T}},$$

along with $\varepsilon_L \sim \hbar/t_{\rm rev}$. Thus, within the stabilizer segment $(0 \leq t \leq t_s)$,

$$\|\rho_a - \tilde{\rho}\|_{\rm tr} \lesssim \frac{t_s w_0^3}{t_{\rm rev}}\sqrt{\frac{\varepsilon_0 t_s}{\hbar}}e^{-\frac{E_J}{k_B T}}. \tag{A15}$$

Combining this result with Eq. (A6) and the triangle inequality $\|\tilde{\rho} - \rho_{\rm rf}\|_{\rm tr} \leq \|\tilde{\rho} - \rho_a\|_{\rm tr} + \|\rho_{\rm rf} - \rho_a\|_{\rm tr}$, and using $t_s \geq t_{\rm rev}$, it follows that

$$\|\rho_{\rm rf} - \tilde{\rho}\|_{\rm tr} \lesssim \frac{t_s}{t_{\rm rev}}w_0^3\sqrt{\frac{\varepsilon_0 t_s}{\hbar}}e^{-\frac{E_J}{k_{\rm B}T}}. \tag{A16}$$

This establishes Eq. (A2), which was our goal.

APPENDIX B: CONFINEMENT IN CODE SUBSPACE

Here, we derive the bounds on the spread of S_2 support quoted in Eqs. (20) and (25).

To recap, our goal is to bound the probability support of $\tilde{\rho}(t)$ in the domain $|S_2| > s$ as a function of s and time t,

$$\tilde{\mathcal{P}}_2(s,t) \equiv {\rm Tr}[\theta(s - S_2)\tilde{\rho}(t)], \tag{B1}$$

where $\tilde{\rho}(t) \equiv e^{-i\tilde{H}t}\rho(0)e^{i\tilde{H}t}$ denotes the evolution generated by the effective Hamiltonian $\tilde{H}$ and coincides with state of the system in the comoving frame, up to an exponentially small correction (bounded in the previous appendix).

1. Derivation of Eq. (20)

We first derive the bound in Eq. (20). To this end, for a given $k > 0$, we introduce the operator

$$w_k \equiv e^{-kS_2}. \tag{B2}$$

The positive semidefiniteness of w_k and $\theta(s - S_2)$ implies that $w_k \geq e^{-ks}\theta(s - S_2)$ for any s. Thus, for any $k > 0$ and $s \in [-1, 1]$,

$$\tilde{\mathcal{P}}_2(s,t) \leq e^{ks}\langle w_k(t)\rangle, \tag{B3}$$

where we have introduced the shorthand $\langle w_k(t)\rangle \equiv {\rm Tr}[w_k\tilde{\rho}(t)]$. We now bound $\langle w_k(t)\rangle$ by considering its equation of motion,

$$\partial_t\langle w_k(t)\rangle = \frac{i}{\hbar}{\rm Tr}\left(\tilde{\rho}(t)[\tilde{H}, w_k]\right). \tag{B4}$$

We recall from Eq. (17) that $\tilde{H} = \tilde{H}_0 + M\varphi_0\bar{\varphi}/L$, with $\tilde{H}_0$ defined in Eq. (18), $\bar{\varphi} \equiv \varphi \bmod \varphi_0$ denoting the quasiflux operator, and $M = {\rm round}(\varphi/\varphi_0)$ denoting the integer-valued well index operator. Using $[\tilde{H}_0, S_2] = [\bar{\varphi}, S_2] = 0$ and $[M, S_2] = -2i\sin(2\pi q/e)$, we thus obtain

$$[\tilde{H}, w_k] = -2ik\frac{\bar{\varphi}\varphi_0}{L}\sin\left(\frac{2\pi q}{e}\right)w_k. \tag{B5}$$

Using that $[\bar{\varphi}, e^{-i2\pi q/e}] = 0$, we thus find that

$$\partial_t\langle w_k(t)\rangle = -\frac{2k\varphi_0}{L\hbar}{\rm Tr}\left(\bar{\varphi}\sin\left[\frac{2\pi q}{e}\right]e^{-\frac{kS_2}{2}}\tilde{\rho}(t)e^{-\frac{kS_2}{2}}\right). \tag{B6}$$

Note that $e^{-kS_2/2}\tilde{\rho}(t)e^{-kS_2/2}$ is a positive semidefinite matrix with trace $\langle w_k(t)\rangle$; we can thus view it as a rescaling of the density matrix $\rho_k(t)$, defined in Eq. (21), i.e.,:

$$\rho_k(t) \equiv \frac{1}{\langle w_k(t)\rangle} e^{-\frac{kS_2}{2}} \tilde{\rho}(t) e^{-\frac{kS_2}{2}}. \tag{B7}$$

Combining Eqs. (B6) and (B7) we thus find that

$$\partial_t \langle w_k(t)\rangle = -k v_k(t) \langle w_k(t)\rangle, \tag{B8}$$

where

$$v_k(t) \equiv \frac{2\varphi_0}{\hbar L} \mathrm{Tr}\left[\rho_k(t)\bar{\varphi} \sin\left(\frac{2\pi q}{e}\right)\right]. \tag{B9}$$

Formally integrating Eq. (B8) yields

$$\langle w_k(t)\rangle = e^{-k\int_0^t ds v_k(s)} \langle w_k(0)\rangle, \tag{B10}$$

implying that

$$\tilde{\mathcal{P}}_2(s,t) \leq e^{k[s+\Delta s_k(t)]} \langle w_k(0)\rangle, \tag{B11}$$

with $\Delta s_k(t) = -k\int_0^t dt' v_k(t')$.

We now recall from Sec. IV that we have assumed the S_2 support of $\rho(0)$ [and hence also $\tilde{\rho}(0)$] to be confined to the region $S_2 \geq s_0$. In this case, $\langle w_k(0)\rangle \leq e^{-ks_0}$, implying that, for any $k \geq 0$,

$$\tilde{\mathcal{P}}_2(s,t) \leq e^{-k[s_0 - s - \Delta s_k(t)]}. \tag{B12}$$

Combining Eqs. (B7), (B9), and (B12), this establishes Eq. (20), which is the goal of this subsection.

2. Derivation of Eq. (25)

Here, we derive Eq. (25). We establish Eq. (25) from Eq. (B11) by fixing $k = k_0$, where $k_0 = 1/2\pi\lambda^2$ [99], and computing $\langle w_{k_0}(0)\rangle$ for a state stabilized by the protocol. To this end, we note that

$$\langle w_{k_0}(0)\rangle = e\int_{-\infty}^{\infty} dx\, p_q(xe) e^{-k_0\cos(2\pi x)}, \tag{B13}$$

where $p_q(x) \equiv \mathrm{Tr}[\delta(q-x)\tilde{\rho}(0)]$ is the charge probability distribution of the system at the onset of the stabilizer segment. Since a free segment maps φ/φ_0 to q/e, $p_q(x)$ is given by the flux probability distribution at the end of the previous stabilizer segment with this rescaling. Using the flux distribution from Eq. (13), we thus find that

$$p_q(x) \approx \frac{e^{-x^2/\lambda^2 e^2}}{\sqrt{2\pi} e\lambda}. \tag{B14}$$

Using the above result, we compute Eq. (B13) via the saddle-point approximation, which is valid when $\lambda \ll 1$ (and hence also $k_0 \gg 1$). For $k = k_0$, the exponent of the integrand in Eq. (B13) attains its maximum around $x = 0$, where it scales as $-1/2\pi^2\lambda^2(1 + \frac{2}{3}\pi^4x^4)$. In the regime $\lambda \ll 1$, this integral is dominated by the contribution near $x = 0$ and thus

$$\langle w_{k_0}(0)\rangle \approx \frac{1}{\sqrt{2\pi}\lambda}\int_{-\infty}^{\infty} dx e^{-\frac{1}{2\pi^2\lambda^2}\left(1+\frac{2}{3}\pi^4x^4\right)}. \tag{B15}$$

Evaluating the integral, we find that

$$\langle w_{k_0}(0)\rangle \lesssim \frac{0.5}{\sqrt{\lambda}} e^{-\frac{1}{2\pi^2\lambda}}. \tag{B16}$$

Inserting this in Eq. (B11), we conclude that

$$\tilde{\mathcal{P}}_2(s,t) \lesssim \frac{0.5}{\sqrt{\lambda}} \exp\left[\frac{-1 + s + \Delta s_{k_0}(t)}{2\pi^2\lambda^2}\right]. \tag{B17}$$

In the limit $\Delta s_{k_0}(t) \ll 1$, and suppressing the subdominant power-law prefactors, we recover $\mathcal{P}_2(s,t) \lesssim \exp\left[(-1+s)/(2\pi^2\lambda^2)\right]$. This establishes Eq. (25), which was the goal of this subsection.

APPENDIX C: BOUND ON LOGICAL ERROR RATE

Here, we establish the bound for the logical error rate quoted in Eq. (26). To recap, we are interested in bounding the change of the logical expectation values in the evolution generated by $\tilde{H}$, after the system has converged to the fixed point in the code subspace (see Sec. IV A); i.e., we seek to bound $|\delta\tilde{\sigma}_i|$, where

$$\delta\tilde{\sigma}_i \equiv \mathrm{Tr}[\tilde{\rho}(t_s)\sigma_i] - \mathrm{Tr}[\tilde{\rho}(0)\sigma_i] \tag{C1}$$

and $\tilde{\rho}(0)$ is the density matrix at the onset of the stabilizer segment, after the system has converged to the fixed point of the protocol, as described in Sec. IV A.

Below, we establish bounds on $\delta\tilde{\sigma}_x, \delta\tilde{\sigma}_y$, and $\delta\tilde{\sigma}_z$ separately. The derivation is quite independent for each logical operator and, for $\delta\tilde{\sigma}_x$ and $\delta\tilde{\sigma}_y$, involves multiple triangle inequalities; we therefore devote a separate subsection to each logical operator, in the order $\delta\tilde{\sigma}_z$ (Sec. C 1), $\delta\tilde{\sigma}_x$ (Sec. C 2), and $\delta\tilde{\sigma}_y$ (Sec. C 3). From these derivations, we obtain the following inequalities:

$$|\delta\tilde{\sigma}_x| \lesssim \frac{t_s}{\lambda^{\frac{3}{2}} t_{\mathrm{rev}}} e^{-\frac{1}{\pi^2\lambda^2}}, \tag{C2}$$

$$|\delta\tilde{\sigma}_y| \lesssim \sqrt{\frac{\varepsilon_0 t_s}{\hbar}} \frac{\kappa^3 t_s^2}{\sqrt{\lambda} t_{\mathrm{rev}}^2} e^{-\frac{E_J}{k_B T}} + \frac{t_s}{\lambda^{\frac{3}{2}} t_{\mathrm{rev}}} e^{-\frac{1}{\pi^2\lambda^2}}, \tag{C3}$$

$$|\delta\tilde{\sigma}_z| \lesssim \sqrt{\frac{\varepsilon_0 t_s}{\hbar}} \frac{\kappa^3 t_s}{t_{\mathrm{rev}}} e^{-\frac{E_J}{k_{\mathrm{B}} T}}, \tag{C4}$$

where $\kappa = \sqrt{\coth(2\varepsilon_0/k_{\mathrm{B}}T)}/\pi\lambda_0$ denotes the dimensionless GKP envelope width and $\varepsilon_0 = \sqrt{4\pi h f_{LC} E_J}$ denotes the characteristic excitation energies in the wells of the cosine potential from the Josephson junction. As in the main text, $x \lesssim y$ indicates that x is bounded from above by y, up to multiplication by some $\mathcal{O}(1)$ constant. In particular, we emphasize that $x \lesssim y$ allows x to be arbitrarily smaller than y.

Using that we work in the regime $\lambda \ll 1$, $t_s \geq t_{\mathrm{rev}}$, and $\lambda^2 \leq \lambda_0^2 + k_{\mathrm{B}}T/\pi^2 E_J$ (see Appendix E), the results above thus imply that

$$|\delta\tilde{\sigma}_i| \lesssim \frac{t_s^2\kappa^3}{t_{\mathrm{rev}}^2\lambda}\sqrt{\frac{\varepsilon_0 t_s}{\hbar}}\exp\left[-\frac{1}{k_B T/E_J + \pi^2\lambda_0^2}\right]. \tag{C5}$$

Suppressing the power-law prefactors, this establishes Eq. (9).

1. Bound on $\delta\tilde{\sigma}_z$

We first establish the bound for $\delta\tilde{\sigma}_z$ in Eq. (C4). The derivation is structured as follows. First, we show that $\delta\tilde{\sigma}_z$ is exponentially close to the change of the expectation of σ_z in the *laboratory frame* over the stabilizer segment. Second, we show that the latter—giving the net flux of probability support between the wells of the Josephson potential—is bounded via an Arrhenius law.

To relate $\delta\tilde{\sigma}_z$ to the change of σ_z in the laboratory frame, we recall that $\|\rho_{\mathrm{rf}}(t) - \tilde{\rho}(t)\|_{\mathrm{tr}} \lesssim \frac{\kappa^3 t_s}{t_{\mathrm{rev}}}\sqrt{\varepsilon_0 t_s/\hbar}e^{-\frac{E_J}{k_B T}}$ [Eq. (A16)], with $\rho_{\mathrm{rf}}(t) \equiv V^\dagger(t)\rho(t)V(t)$ and $V(t)$ denoting the transformation to the comoving frame introduced in Eq. (14). Next, we note that V commutes with σ_z, implying that $\mathrm{Tr}[\rho_{\mathrm{rf}}(t)\sigma_z] = \mathrm{Tr}[\rho(t)\sigma_z]$. We now have

$$|\mathrm{Tr}[AB]| \leq \|A\|_{\mathrm{tr}}\|B\|, \tag{C6}$$

where, for any operator A, $\|A\|_{\mathrm{tr}}$ and $\|A\|$ denote its trace and singular-value norms, respectively, $\|A\|_{\mathrm{tr}} \equiv \mathrm{Tr}[\sqrt{A^\dagger A}]$ and $\|A\| \equiv \sup_{\psi,\phi}|\langle\psi|A|\phi\rangle|/\sqrt{|\langle\psi|\psi\rangle\langle\phi|\phi\rangle|}$. Using $\|\sigma_z\| = 1$, we thus find that

$$|\mathrm{Tr}[\rho(t)\sigma_z] - \mathrm{Tr}[\tilde{\rho}(t)\sigma_z]| \lesssim \frac{\kappa^3 t_s}{t_{\mathrm{rev}}}\sqrt{\frac{\varepsilon_0 t_s}{\hbar}}e^{-\frac{E_J}{k_B T}}. \tag{C7}$$

We next note that $\mathrm{Tr}[\rho(t)\sigma_z]$ gives the net imbalance of probability weight between the even and odd wells of the cosine potential from the Josephson junction in the state ρ. The flow of probability support between the wells is suppressed via the Arrhenius law, i.e., is exponentially small in $2E_J/k_B T$. For example, Ref. [55] has shown that the flow rate of probability support between even and odd wells is of order $\varepsilon_0/\hbar e^{-2\frac{E_J}{k_B T}}$, leading to

$$\partial_t \mathrm{Tr}[\rho\sigma_z] \sim \frac{\varepsilon_0}{\hbar}e^{-\frac{2E_J}{k_B T}}. \tag{C8}$$

Using the triangle inequality, $|f(t) - f(0)| \leq \int_0^t dt' |\partial_t f(t')|$, it follows that

$$|\mathrm{Tr}[\rho(t)\sigma_z] - \mathrm{Tr}[\rho(0)\sigma_z]| \lesssim \frac{\varepsilon_0 t}{\hbar}e^{-\frac{2E_J}{k_B T}}. \tag{C9}$$

By combining the above result with Eq. (C7) and using the triangle inequality, we thus obtain

$$|\delta\tilde{\sigma}_z| \lesssim \frac{\kappa^3 t_s}{t_{\mathrm{rev}}}\sqrt{\frac{\varepsilon_0 t_s}{\hbar}}e^{-\frac{E_J}{k_B T}}, \tag{C10}$$

which was what we wanted to show.

2. Bound on $\delta\tilde{\sigma}_x$

We next establish the bound on $|\delta\tilde{\sigma}_x|$ in Eq. (C2). The derivation has two steps. First, introduce a *regularized* logical operator:

$$\tau_x \equiv f_r(q/e), \tag{C11}$$

where $f_r(x)$ (plotted in Fig. 10) is given by

$$f_r(x) = \begin{cases} 1, & |x| < 1/2 - \alpha, \\ (1/2 - |x|)/\alpha, & |x| > 1/2 - \alpha, \end{cases} \tag{C12}$$

where $\alpha = \lambda/\sqrt{2}$ and $f_r(x) = -f_r(x+1)$ defines $f_r(x)$ for all other values of x. The function $f_r(x)$ can be viewed as a continuous generalization of the crenellation function $\Xi(x)$. In Sec. C 2 a, we show that, for state $\tilde{\rho}(t)$ stabilized with the protocol, the expectation values of τ_x and σ_x coincide up to exponentially small deviations:

$$|\mathrm{Tr}[\tilde{\rho}(t)\sigma_x] - \mathrm{Tr}[\tilde{\rho}(t)\tau_x]| \lesssim \frac{1}{\sqrt{\lambda}}e^{-\frac{1}{\pi^2\lambda^2}}. \tag{C13}$$

Second, in Sec. C 2 b, we show that $\mathrm{Tr}[\tilde{\rho}(t)\tau_x]$ is near constant throughout the stabilizer segment:

$$|\mathrm{Tr}[\tilde{\rho}(t)\tau_x] - \mathrm{Tr}[\tilde{\rho}(0)\tau_x]| \lesssim \frac{t_s}{\lambda^{\frac{3}{2}} t_{\mathrm{rev}}}e^{-\frac{1}{\pi^2\lambda^2}}. \tag{C14}$$

Equation (C2) follows when combining these two results along with $\lambda \ll 1$, $t_s \geq t_{\mathrm{rev}}$ and using the triangle inequality.

We now proceed to derive Eqs. (C13) and (C14). Throughout the remainder of this section, we will suppress the time dependence of all quantities, unless otherwise noted.

a. Derivation of Eq. (C13)

To establish Eq. (C13), we first note that $f_r(x) = \Xi(x)$ for $|x| < 1/2 - \alpha$. As a result, $\sigma_x - \tau_x$ only has support in the region $S_2 \leq s_\alpha$, with $s_\alpha \equiv -\cos(2\pi\alpha)$.

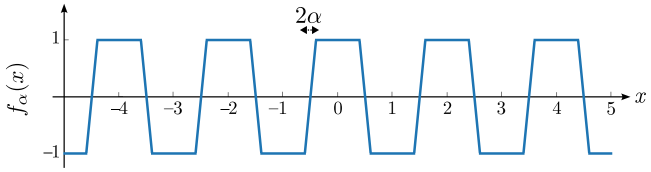

FIG. 10. A plot of the function $f_r(x)$.

Hence, $\sigma_x - \tau_x = P_2(s_\alpha)(\sigma_x - \tau_x)P_2(s_\alpha)$, where $P_2(s) \equiv \theta(s - S_2)$, implying that

$$|\mathrm{Tr}[\tilde\rho\tau_x] - \mathrm{Tr}[\tilde\rho\sigma_x]| = |\mathrm{Tr}[P_2(s_\alpha)\tilde\rho P_2(s_\alpha)(\sigma_x - \tau_x)]|. \tag{C15}$$

Using $|\mathrm{Tr}[AB]| \leq \|A\|_{\mathrm{tr}}\|B\|$, we find that

$$|\mathrm{Tr}[\tilde\rho\tau_x] - \mathrm{Tr}[\tilde\rho\sigma_x]| \leq \|P_2(s_\alpha)\tilde\rho P_2(s_\alpha)\|_{\mathrm{tr}}\|\sigma_x - \tau_x\|. \tag{C16}$$

Since $\sigma_x - \tau_x = \Xi(q/e) - f_r(q/e)$, the eigenvalues of $\sigma_x - \tau_x$ are bounded by 1, implying that $\|\sigma_x - \tau_x\| \leq 1$. Moreover, since $P_2(s_\alpha)\tilde\rho P_2(s_\alpha)$ is positive semidefinite, $\|A\|_{\mathrm{tr}} = \mathrm{Tr}[A]$ for positive semidefinite A, and $P_2^2(s) = P_2(s)$, we find that $\|P_2(s_\alpha)\tilde\rho P_2(s_\alpha)\|_{\mathrm{tr}} = \mathrm{Tr}[\tilde\rho P_2(s_\alpha)]$. Recognizing $\mathrm{Tr}[\tilde\rho P_2(s_\alpha)] = \mathcal{P}_2(s_\alpha)$, with $\mathcal{P}_2(s_\alpha)$ defined above Eq. (20), we conclude that

$$|\mathrm{Tr}[\tilde\rho\tau_x] - \mathrm{Tr}[\tilde\rho\sigma_x]| \leq \mathcal{P}_2(s_\alpha). \tag{C17}$$

Next, we recall from Eq. (B17) that for states stabilized by the protocol, and with $\Delta s_{k_0}(t) \ll 1$,

$$\mathcal{P}_2(s_\alpha) \lesssim \frac{1}{\sqrt{\lambda}}e^{-\frac{1-s_\alpha}{2\pi^2\lambda^2}}, \tag{C18}$$

where $s_\alpha \equiv -\cos(2\pi\alpha)$ and with $\mathcal{O}(1)$ prefactors suppressed. Since $\alpha = \lambda/\sqrt{2\pi}$ and we work in the regime $\lambda \ll 1$, we find that $s_\alpha \approx -1 + \pi\lambda^2$, implying that

$$\mathcal{P}_2(s_\alpha) \lesssim \frac{1}{\sqrt{\lambda}}e^{-\frac{1}{\pi^2\lambda^2}}, \tag{C19}$$

where we have again suppressed $\mathcal{O}(1)$ prefactors. Using this in Eq. (C17), we recover Eq. (C13), which was our goal.

b. Derivation of Eq. (C14)

To establish Eq. (C14), we consider the equation of motion for $\mathrm{Tr}[\tau_x\tilde\rho]$, which can be written

$$\partial_t\mathrm{Tr}[\tilde\rho\tau_x] = -\frac{i}{\hbar}\mathrm{Tr}\left([\tau_x, \tilde H]\tilde\rho\right), \tag{C20}$$

where $\tilde H$ is given in Eq. (17). To evaluate the commutator, we recall $\tilde H = \tilde H_0 + M\varphi_0\bar\varphi/L$, where $M = \mathrm{round}(\varphi/\varphi_0)$, $\bar\varphi = \varphi - M\varphi_0$, while $\bar H$—defined in Eq. (18)—is exclusively a function of $\bar\varphi$, q, H_R, and Q_{R}. Since τ_x is a $2e$-periodic function of q, it commutes with any φ_0-periodic function of φ, i.e., operators that can be written as functions of $\bar\varphi$. As a result, $[\tau_x, \bar\varphi] = [\tau_x, \tilde H_0] = 0$, implying that $[\tau_x, \tilde H] = [\tau_x, M]\varphi_0\bar\varphi/L$. We next note that $[\tau_x, M] = 1/\varphi_0[\tau_x, \varphi - \bar\varphi]$, implying that $[\tau_x, M] = 1/\varphi_0[\tau_x, \varphi]$. Since $[q, \varphi] = -i\hbar$, we thus conclude that

$$[\tau_x, M] = -i\frac{\hbar}{e}f_r'(q/e). \tag{C21}$$

Thus we find [100]

$$[\tau_x, \tilde H] = i\frac{\bar\varphi\hbar}{Le}f_\alpha'(q/e). \tag{C22}$$

We now use that

$$f_\alpha'(x) = \frac{X}{\alpha}, \quad X \equiv \sum_z \theta(\alpha - |q/e - z - 1/2|)(-1)^z. \tag{C23}$$

Using this together with Eq. (C20), we find

$$\partial_t\mathrm{Tr}[\tilde\rho\tau_x] = \frac{1}{eL\alpha}\mathrm{Tr}[\tilde\rho\bar\varphi X]. \tag{C24}$$

Note that X only has support in the subspace with $S_2 < s_\alpha$. Thus $X = P_2(s_\alpha)XP_2(s_\alpha)$. We also recall $[\bar\varphi, S_2] = 0$ [57], implying that $[\bar\varphi, P_2(s)] = 0$. As a result, $\mathrm{Tr}[\tilde\rho\bar\varphi X] = \mathrm{Tr}[P_2(s_\alpha)\tilde\rho P_2(s_\alpha)\bar\varphi X]$. Using $|\mathrm{Tr}[AB]| \leq \|A\|_{\mathrm{tr}}\|B\|$ along with $\|P_2(s_\alpha)\tilde\rho P_2(s_\alpha)\|_{\mathrm{tr}} = \tilde{\mathcal{P}}_2(s_\alpha)$ and $\|\bar\varphi X\| \leq \|\bar\varphi\|\|X\| = \varphi_0/2$, we conclude that

$$|\partial_t\mathrm{Tr}[\tilde\rho\tau_x]| \leq \frac{\varphi_0}{2eL\alpha}\tilde{\mathcal{P}}_2(s_\alpha). \tag{C25}$$

To simplify the prefactor, we finally use that $\varphi_0/e = h/2e^2$, which coincides with the resonator impedance $\sqrt{L/C}$. Also using $\sqrt{LC} = t_{\mathrm{rev}}$, we find that $L = t_{\mathrm{rev}}\varphi_0/e$. Thus,

$$|\partial_t\mathrm{Tr}[\tilde\rho\tau_x]| \leq \frac{\mathcal{P}_2(s_\alpha)}{\alpha t_{\mathrm{rev}}}. \tag{C26}$$

Recalling that $\alpha = \lambda/\sqrt{2\pi}$ and using Eq. (C19), we thus find that

$$|\partial_t\mathrm{Tr}[\tilde\rho\tau_x]| \lesssim \frac{1}{\lambda^{\frac{3}{2}}t_{\mathrm{rev}}}e^{-\frac{1}{\pi^2\lambda^2}}, \tag{C27}$$

where we have also used $\sqrt{2\pi} \sim 1$. We obtain Eq. (C14) by integrating over time, using the triangle inequality. This concludes this subsection.

3. Bound on $\delta\tilde{\sigma}_y$

We finally establish the bound on $\delta\tilde{\sigma}_y(t)$ in Eq. (C3). The derivation proceeds in two steps. First, we introduce a scalar quantity $\mathcal{Y}(t)$, which we show is approximately identical to $\mathrm{Tr}[\tilde{\rho}(t)\sigma_y]$ (Sec. C 3 a). Specifically,

$$\mathcal{Y}(t) \equiv i\mathrm{Tr}[\tau_x U(t) V^\dagger(t)\sigma_z\rho(0)V(t)U^\dagger(t)], \tag{C28}$$

where $U(t) = e^{-iH_s t}$ is the evolution operator in the laboratory frame and $V(t)$ generates the transformation to the comoving frame [Eq. (14)]. In Sec. C 3 a, we show that

$$|\mathcal{Y}(t) - \mathrm{Tr}[\tilde{\rho}(t)\sigma_y]| \lesssim \sqrt{\frac{\varepsilon_0 t}{\hbar}}\frac{\kappa^3 t_s e^{-\frac{E_J}{k_B T}}}{t_{\mathrm{rev}}} + \frac{e^{-\frac{1}{\pi^2\lambda^2}}}{\sqrt{\lambda}}. \tag{C29}$$

Second, in Sec. C 3 b, we show that $\mathcal{Y}(t)$ is near constant over the stabilizer segment:

$$|\mathcal{Y}(t_s) - \mathcal{Y}(0)| \lesssim \sqrt{\frac{\varepsilon_0 t_s}{\hbar}}\left[\frac{\kappa^3 t_s^2 e^{-\frac{E_J}{k_{\mathrm{B}}T}}}{\sqrt{\lambda}t_{\mathrm{rev}}^2} + \frac{t_s e^{-\frac{1}{\pi^2\lambda^2}}}{\lambda^{\frac{3}{2}} t_{\mathrm{rev}}}\right]. \tag{C30}$$

Combining these two results via the triangle inequality and using $t_s \geq t_{\mathrm{rev}}, t$ and $\lambda \ll 1$, we establish the bound on $\delta\tilde{\sigma}_y$ quoted in Eq. (C3).

The remainder of this subsection is devoted to deriving Eq. (C29) (Sec. C 3 a) and Eq. (C30) (C 3 b). In this discussion, we suppress the time dependence of all quantities for brevity.

a. Derivation of Eq. (C29)

To establish Eq. (C29), we first use the triangle inequality along with $\sigma_y = i\sigma_x\sigma_z$ to write

$$|\mathcal{Y} - \mathrm{Tr}[\tilde{\rho}\sigma_y]| \leq |\mathcal{Y} - i\mathrm{Tr}[\tilde{\rho}\tau_x\sigma_z]| + |i\mathrm{Tr}[\tilde{\rho}(\tau_x\sigma_z - \sigma_x\sigma_z)|. \tag{C31}$$

We now bound the two terms on the right-hand side separately.

To bound $|\mathcal{Y} - i\mathrm{Tr}[\tilde{\rho}\tau_x\sigma_z]|$, we note that $Y - i\mathrm{Tr}[\tilde{\rho}\tau_x\sigma_z] = i\mathrm{Tr}[\tau_x(Z - \sigma_z\tilde{\rho})]$, where

$$Z \equiv UV^\dagger\sigma_z\rho_0 VU^\dagger. \tag{C32}$$

This follows from Eq. (C28). Using $|\mathrm{Tr}[AB]| \leq \|A\|_{\mathrm{tr}}\|B\|$ along with $\|\tau_x\| = 1$, we find that

$$|\mathcal{Y} - \mathrm{Tr}[\tilde{\rho}\sigma_y]| \leq \|Z - \sigma_z\tilde{\rho}\|_{\mathrm{tr}}. \tag{C33}$$

To bound the right-hand side, we introduce the ancillary density matrix $\rho_a \equiv UV^\dagger\rho_0 VU^\dagger$, which has also been considered in Appendix A [see Eq. (A4)]. Using the triangle inequality, we find that

$$\|Z - \sigma_z\tilde{\rho}\|_{\mathrm{tr}} \leq \|Z - \sigma_z\rho_a\|_{\mathrm{tr}} + \|\sigma_z\rho_a - \sigma_z\tilde{\rho}\|_{\mathrm{tr}}. \tag{C34}$$

We bound the second term on the right-hand side above using $\|AB\|_{\mathrm{tr}} \leq \|A\|\|B\|_{\mathrm{tr}}$ [101] and $\|\sigma_z\| = 1$, implying that $\|\sigma_z\rho_a - \sigma_z\tilde{\rho}\|_{\mathrm{tr}} \leq \|\rho_a - \tilde{\rho}\|_{\mathrm{tr}}$. We now recall from Eq. (A15) that

$$\|\rho_a - \tilde{\rho}\|_{\mathrm{tr}} \lesssim \frac{t_s}{t_{\mathrm{rev}}} w_0^3\sqrt{\frac{\varepsilon_0 t_s}{\hbar}}e^{-\frac{E_J}{k_{\mathrm{B}}T}}, \tag{C35}$$

where w_0 denotes the φ support range of ρ_0 in units of φ_0, such that ρ_0 has φ support confined within the interval $[-w_0\varphi_0, w_0\varphi_0]$. Since we consider the dynamics of stabilized states, the flux distribution of ρ_0 has a Gaussian envelope of characteristic width κ (see Sec. IV A), implying that we may set $w_0 \sim \kappa$ [97]. Again using that $\|AB\|_{\mathrm{tr}} \leq \|A\|\|B\|_{\mathrm{tr}}$ and $\|\sigma_z\| = 1$, we find that

$$\|\sigma_z\tilde{\rho} - \sigma_z\rho_a\|_{\mathrm{tr}} \lesssim \frac{t_s\kappa^3}{t_{\mathrm{rev}}}\sqrt{\frac{\varepsilon_0 t_s}{\hbar}}e^{-\frac{E_J}{k_{\mathrm{B}}T}}. \tag{C36}$$

To bound the first term on the right-hand side of Eq. (C34), we use the definition of Z in Eq. (C32) to write

$$\|Z - \sigma_z\rho_a\|_{\mathrm{tr}} = \|[\sigma_z, U]V^\dagger\rho_0\|_{\mathrm{tr}}. \tag{C37}$$

Here, we have used that $\|\mathcal{U}X\|_{\mathrm{tr}} = \|X\|_{\mathrm{tr}}$ for any unitary operator $\mathcal{U}$ and $[V^\dagger, \sigma_z] = 0$. We next use the inequality in Eq. (A3), noting that the right-hand side above is of the same form as the left-hand side in Eq. (A3), with $g(x) = e^{-ix^2\varepsilon_L t/\hbar}$ and $f(x) = (-1)^x$. Using that $\|f\| = \|g\| = 1$, we find that

$$\|S - \sigma_z\rho_a\|_{\mathrm{tr}} \lesssim \kappa\sqrt{\frac{\varepsilon_0 t}{\hbar}}e^{-\frac{E_J}{k_{\mathrm{B}}T}}. \tag{C38}$$

Combining this with Eq. (C33) and (C36), we obtain

$$|\mathcal{Y} - i\mathrm{Tr}[\tilde{\rho}\tau_x\sigma_z]| \lesssim \frac{t_s\kappa^3}{t_{\mathrm{rev}}}\sqrt{\frac{\varepsilon_0 t_s}{\hbar}}e^{-\frac{E_J}{k_B T}}. \tag{C39}$$

This bounds the first term on the right-hand side of Eq. (C31).

We next bound the second term on the right-hand side of Eq. (C31), $|\mathrm{Tr}[\tilde{\rho}(\tau_x\sigma_z - \sigma_x\sigma_z)|$. We first recall that $\sigma_x - \tau_x = P_2(s_\alpha)(\sigma_x - \tau_x)P_2(s_\alpha)$, where $P_2(s) \equiv \theta(s - S_2)$ [see the text above Eq. (C15)]. Thus,

$$|Tr[(\tau_x - \sigma_x)\sigma_z\tilde{\rho}]| = |\mathrm{Tr}[\tilde{\rho}P_2(s_\alpha)(\sigma_x - \tau_x)P_2(s_\alpha)\sigma_z]|. \tag{C40}$$

Note that $P_2(s)$ is a function of S_2 and, hence, $[P_2(s), \sigma_z] = 0$. Using this fact, along with $|\mathrm{Tr}(AB)| \leq \|A\|_{\mathrm{tr}}\|B\|$,

$\|\sigma_z(\sigma_x - \tau_x)\| \leq 1$, and $\|P_2(s_\alpha)\tilde{\rho}P_2(s_\alpha)\|_{\rm tr} = \mathcal{P}_2(s_\alpha)$, we find that

$$|{\rm Tr}[(\tau_x - \sigma_x)\sigma_z\tilde{\rho}]| \leq \mathcal{P}_2(s_\alpha). \tag{C41}$$

Since $\alpha = \lambda/\sqrt{2\pi}$ and $\mathcal{P}_2(s_\alpha) \lesssim \frac{1}{\sqrt{\lambda}}e^{-\frac{1}{\pi^2\lambda^2}}$ [Eq. (C19)], we find that

$$|{\rm Tr}[(\tau_x - \sigma_x)\sigma_z\tilde{\rho}]| \lesssim \frac{1}{\sqrt{\lambda}}e^{-\frac{1}{\pi^2\lambda^2}}. \tag{C42}$$

Combining Eqs. (C42), (C39), and (C31), we obtain

$$|Y - {\rm Tr}[\tilde{\rho}\sigma_y]| \lesssim \frac{\kappa^3 t_s}{t_{\rm rev}}\sqrt{\frac{\varepsilon_0 t}{\hbar}}e^{-\frac{E_J}{k_{\rm B}T}} + \frac{1}{\sqrt{\lambda}}e^{-\frac{1}{\pi^2\lambda^2}}. \tag{C43}$$

This establishes Eq. (C29), which was the goal of this subsection.

b. Derivation of Eq. (C30)

We next derive Eq. (C30), which bounds the change of $\mathcal{Y}$ over the stabilizer segment. To this end, we note from Eq. (C32) that

$$\partial_t\mathcal{Y} = {\rm Tr}[\tau_x\partial_t Z], \tag{C44}$$

with $Z \equiv UV^\dagger\sigma_z\rho_0 VU^\dagger$. defined in Eq. (C32). Using $V = e^{-i\varepsilon_L tM^2/\hbar}$, $U = e^{-itH_s}$ and $\tilde{H} = H_s - \varepsilon_L M^2$, where $M \equiv$ round(φ/φ_0), explicit computation yields

$$\begin{aligned}\partial_t Z &= -\frac{i}{\hbar}[\tilde{H}, Z] + \delta\dot{Z}, \quad \text{where}\\ \delta\dot{Z} &\equiv \frac{i\varepsilon_L}{\hbar}[(UM^2U^\dagger - M^2), Z].\end{aligned} \tag{C45}$$

Thus,

$$\partial_t Y = \frac{i}{\hbar}{\rm Tr}[S[\tilde{H}, \tau_x]] + {\rm Tr}[\tau_x\delta\dot{Z}]. \tag{C46}$$

We now bound the two terms on the right-hand side above separately.

We first bound ${\rm Tr}[\tau_x\delta\dot{Z}]$. We first note that, since $|{\rm Tr}[AB]| \leq \|A\|_{\rm tr}\|B\|$ and $\|\tau_x\| = 1$, $|{\rm Tr}[\tau_x\delta\dot{Z}]| \leq \|\delta\dot{Z}\|_{\rm tr}$. To bound $\|\delta\dot{Z}\|_{\rm tr}$, we note from the definition of Z in Eq. (C32) that

$$\delta\dot{Z} = \frac{i\varepsilon_L}{\hbar}\left([U, M^2]V^\dagger\sigma_z\rho_0 VU^\dagger + UV^\dagger\sigma_z\rho_0 V[U, M^2]\right). \tag{C47}$$

Using $|{\rm Tr}[\tau_x\delta\dot{Z}]| \leq \|\delta\dot{Z}\|_{\rm tr}$ along with the triangle inequality, we thus find that

$$|{\rm Tr}[\tau_x\delta\dot{Z}]| \leq \frac{\varepsilon_L}{\hbar}\|[U, M^2]V^\dagger\sigma_z\rho_0\|_{\rm tr} + \frac{\varepsilon_L}{\hbar}\|[U^\dagger, M^2]V\rho_0\|_{\rm tr}. \tag{C48}$$

We can use Eq. (A3) to bound the two terms on the right, with $f(x) = x^2$ and $g(x) = e^{-i\varepsilon_L tx^2/\hbar - i\pi x}$ and $g(x) = e^{-i\varepsilon_L tx^2/\hbar}$ for the first and second terms, respectively. Using $\|f\| = w_0^2 \sim \kappa^2$ (see Note [97]), this analysis yields

$$|{\rm Tr}[\tau_x\delta\dot{Z}]| \leq \frac{\kappa^3}{t_{\rm rev}}\sqrt{\frac{\varepsilon_0 t}{\hbar}}e^{-\frac{E_J}{k_B T}}. \tag{C49}$$

We next bound the first term on the right-hand side of Eq. (C46), $(i/\hbar){\rm Tr}([\tilde{H}_{\rm s}, \tau_x]S)$. To this end, we first recall $[\tilde{H}, \tau_x] = (\bar{\varphi}\hbar/Le\alpha)X$, where $X \equiv \sum_z\theta(\alpha - |q/e - z - 1/2|)(-1)^z$ [see Eqs. (C22) and (C23)]. Thus,

$$ {\rm Tr}[Z[\tilde{H}, \tau_x]] = \frac{\hbar}{Le\alpha}{\rm Tr}[Z\bar{\varphi}X]. \tag{C50}$$

Next, we insert $Z = \sigma_z\tilde{\rho} + (Z - \sigma_z\tilde{\rho})$, resulting in

$${\rm Tr}[Z[\tilde{H}, \tau_x]] = \hbar\frac{{\rm Tr}[\sigma_z\tilde{\rho}\bar{\varphi}X]}{Le\alpha} + \hbar\frac{{\rm Tr}[(Z - \sigma_z\tilde{\rho})\bar{\varphi}X]}{Le\alpha}. \tag{C51}$$

We first bound the second term in the above numerator. To this end, we use $|{\rm Tr}[AB]| \leq \|A\|_{\rm tr}\|B\|$ and $\|\bar{\varphi}X\| \leq \|X\|\|\bar{\varphi}\| = \varphi_0/2$, finding that

$$|{\rm Tr}[\bar{\varphi}X(Z - \sigma_z\tilde{\rho})]| \lesssim \frac{\varphi_0}{2}\|(Z - \sigma_z\tilde{\rho})\|_{\rm tr}. \tag{C52}$$

Next, we use the triangle inequality,

$$\|(Z - \sigma_z\tilde{\rho})\|_{\rm tr} \leq \|(Z - \sigma_z\rho_a)\|_{\rm tr} + \|\sigma_z(\tilde{\rho} - \rho_a)\|_{\rm tr}. \tag{C53}$$

Recalling from Eqs. (C38) and (C36) that

$$\|(Z - \sigma_z\rho_a)\|_{\rm tr} \lesssim \kappa\sqrt{\frac{\varepsilon_0 t}{\hbar}}e^{-\frac{E_J}{k_B T}}, \tag{C54}$$

$$\|\sigma_z(\tilde{\rho} - \rho_a)\|_{\rm tr} \lesssim \frac{t\kappa^3}{t_{\rm rev}}\sqrt{\frac{\varepsilon_0 t}{\hbar}}e^{-\frac{E_J}{k_B T}}, \tag{C55}$$

we thus find that

$$|\mathrm{Tr}[(Z-\sigma_z\tilde{\rho})\bar{\varphi}X]| \lesssim \frac{\varphi_0 t\kappa^3}{2t_{\mathrm{rev}}}\sqrt{\frac{\varepsilon_0 t}{\hbar}}e^{-\frac{E_J}{k_B T}}. \tag{C56}$$

We now bound the first term on the right-hand side of Eq. (C51). To this end, we exploit that X only has support for $S_2 \leq s_\alpha$, implying that $X = P_2(s_\alpha)XP_2(s_\alpha)$. Also using $|\mathrm{Tr}[AB]| \leq \|A\|\|B\|_{\mathrm{tr}}$ along with $[P_2(s_\alpha),\varphi] = [P_2(s_\alpha),\sigma_z] = 0$ and $\|P_2(s)\tilde{\rho}P_2(s)\|_{\mathrm{tr}} = \mathcal{P}_2(s)$, we find that

$$|\mathrm{Tr}[\sigma_z\tilde{\rho}\bar{\varphi}X]| \leq \mathcal{P}_2(s_\alpha)\frac{\varphi_0}{2}. \tag{C57}$$

Recalling that $\mathcal{P}_2(s_\alpha) \lesssim \frac{1}{\sqrt{\lambda}}e^{-\frac{1}{\pi^2\lambda^2}}$ [Eq. (C19)], we obtain

$$|\mathrm{Tr}[\sigma_z\tilde{\rho}\bar{\varphi}X]| \lesssim \frac{\varphi_0}{2\sqrt{\lambda}}e^{-\frac{1}{\pi^2\lambda^2}}. \tag{C58}$$

Combining Eqs. (C56) and (C58) with Eq. (C51), and recalling $\alpha = \lambda/\sqrt{2\pi}$, we conclude that

$$\frac{1}{\hbar}|\mathrm{Tr}[Z[\tilde{H}_s,\tau_x]]| \lesssim \frac{\varphi_0}{Le}\left[\sqrt{\frac{\varepsilon_0 t}{\hbar}}\frac{\kappa^3 te^{-\frac{E_J}{k_{\mathrm{B}}T}}}{\sqrt{\lambda}t_{\mathrm{rev}}} + \frac{e^{-\frac{1}{\pi^2\lambda^2}}}{\lambda^{\frac{3}{2}}}\right]. \tag{C59}$$

Using $\varphi_0/Le = 1/L(\sqrt{L}/\sqrt{C}) = 1/t_{\mathrm{rev}}$ and combining the above result with Eqs. (C49) and (C46), we find that

$$|\partial_t\mathcal{Y}| \lesssim \sqrt{\frac{\varepsilon_0 t}{\hbar}}\frac{\kappa^3(1+t/\sqrt{\lambda}t_{\mathrm{rev}})}{t_{\mathrm{rev}}}e^{-\frac{E_J}{k_{\mathrm{B}}T}} + \frac{e^{-\frac{1}{\pi^2\lambda^2}}}{\lambda^{\frac{3}{2}}t_{\mathrm{rev}}}. \tag{C60}$$

Integrating the right-hand side from $t=0$ to $t=t_s$ and using $\kappa \gg 1$, $\lambda \ll 1$, and $t_s \geq t_{\mathrm{rev}}$, we obtain Eq. (C30), which was the goal of this subsection.

APPENDIX D: DERIVATION OF EQ. (A3)

Here, we derive Eq. (A3), which is used in Appendixes A and C. Specifically, we consider an initial state ρ_0 that is confined inside the wells of the cosine potential from the Josephson junctions (see Sec. IV) and has its φ support confined to a finite interval, $|\varphi| \leq w_0\varphi_0$, where $w_0 \ll E_J/hf_{LC}$. Below, we show that for this state, and for any two functions f and g of $M = \mathrm{round}(\varphi/\varphi_0)$,

$$\|[U(t),f(M)]g(M)\rho_0\|_{\mathrm{tr}} \lesssim \|f\|\|g\|w_0\sqrt{\frac{\varepsilon_0 t}{\hbar}}e^{-\frac{E_J}{k_B T}}, \tag{D1}$$

where we have suppressed $\mathcal{O}(1)$ prefactors, $\|g\| = \max_{|x|\leq w_0}|g(x)|$, and $U(t) =^{-iH_{\mathrm{s}}t}$ is the evolution operator of the combined circuit-resistor system during the stabilizer segment.

To establish Eq. (D1), we first introduce the shorthand for the argument on the left-hand side above,

$$A \equiv [U(t),f(M)]g(M)\rho_0. \tag{D2}$$

Our goal is thus to bound $\|A\|_{\mathrm{tr}}$. To this end, we first insert $1 = \sum_z P_z$, where $P_z = \theta([z+1/2]-\varphi)\theta(\varphi-[z-1/2])$, to obtain

$$A = \sum_w\sum_{z\neq w}P_zU(t)P_w\rho_0[f(z)-f(w)]g(w), \tag{D3}$$

where $\sum_{z\neq w}$ denotes the sum over all integers z between $-w_0$ and w_0 *distinct* from w, while $\sum_w$ implicitly sums between $-w_0$ and w_0. Next, we use that for any operator $\mathcal{O}$, $\|\mathcal{O}\rho\|_{\mathrm{tr}} \leq \sqrt{\mathrm{Tr}[\mathcal{O}^\dagger\mathcal{O}\rho]}$ [102], leading to

$$\|A\|_{\mathrm{tr}} \leq \sum_w\sum_{z\neq w}|g(w)|\sqrt{J_{wz}[f(z)-f(w)]^2}. \tag{D4}$$

where $J_{wz} \equiv \mathrm{Tr}(UP_w\rho_0P_wU^\dagger P_z)$. Next, we use that $|f(z)-f(w)| \leq 2\|f\|$ and $|g(w)| \leq \|g\|$ to write

$$\|A\|_{\mathrm{tr}} \leq 2\|f\|\|g\|\sum_w\sum_{z\neq w}\sqrt{J_{wz}}. \tag{D5}$$

We recognize J_{wz} as the total probability flow from well w to well z over the time interval from 0 to t. Due to the energy barrier of order $2E_J$ between the wells, the rate of probability support escaping well w is of order $p_w e^{-2\frac{E_J}{k_{\mathrm{B}}T}}\frac{\varepsilon_0}{\hbar}$, with $p_w \equiv \mathrm{Tr}[P_w\rho_0]$ denoting the initial probability weight in well w [55]. As a result,

$$\sum_{z\neq w}|J_{wz}| \lesssim e^{-2\frac{E_J}{k_BT}}\varepsilon_0 tp_w/\hbar. \tag{D6}$$

Using that the sum runs over $2w_0+1$ terms and that, for any vector $(v_1,\ldots v_N)$, $\sum_{i=1}^N\sqrt{|v_i|} \leq \sqrt{N}\sqrt{\sum_i|v_i|}$ (a consequence of the Cauchy-Schwartz inequality), we thus find that

$$\sum_{z\neq w}\sqrt{J_{wz}} \lesssim e^{-\frac{E_J}{k_{\mathrm{B}}T}}\sqrt{\frac{\varepsilon_0 t}{\hbar}}\sqrt{p_w}\sqrt{w_0}. \tag{D7}$$

Using $\sum_{i=1}^N\sqrt{|v_i|} \leq \sqrt{N}\sqrt{\sum_i|v_i|}$ again, along with $\sum_w p_w = 1$, we find that $\sum_w\sqrt{p_w} \lesssim \sqrt{w_0}$. Thus,

$$\sum_w\sum_{z\neq w}\sqrt{J_{wz}} \lesssim e^{-\frac{E_J}{k_BT}}\sqrt{\frac{\varepsilon_0 t}{\hbar}}w_0. \tag{D8}$$

Combining this with Eq. (D5), we obtain

$$\|A\|_{\mathrm{tr}} \lesssim \|f\|\|g\|e^{-\frac{E_J}{k_BT}}\sqrt{\frac{\varepsilon_0 t}{\hbar}}w_0. \tag{D9}$$

This establishes Eq. (D1), which was the goal of this appendix.

APPENDIX E: INEQUALITY FOR SQUEEZING PARAMETER

Here, we show that the thermally renormalized GKP squeezing parameter, $\lambda \equiv \sqrt{\coth(2\varepsilon_0/k_B T)}\lambda_0$, satisfies

$$\lambda^2 \leq \frac{k_B T}{\pi^2 E_J} + \lambda_0^2, \tag{E1}$$

where $\varepsilon_0 = \sqrt{4\pi h f_{LC} E_J}$ denotes the characteristic excitation energies in the wells of the Josephson potential and $\lambda_0 \equiv \left(h f_{LC}/4\pi^3 E_J\right)^{1/4}$ denotes the zero-point fluctuation of flux in these wells, in units of φ_0. This result is used in Appendix C. To this end, we use $\coth(x) \leq 1 + x^{-1}$, implying $\lambda^2 \leq \lambda_0^2 + \lambda_0^2 k_B T/\varepsilon_0$. Eq. (E1) follows by inserting $\varepsilon_0 = 4\pi^2\lambda_0^2 E_J$ and using $4\pi^2 \geq \pi^2$. Note also that a tighter bound can be established using $\coth(x) \leq \sqrt{1 + x^{-2}}$, leading to $\lambda^2 \leq \sqrt{\lambda_0^4 + (4\pi^2 E_J/k_\mathrm{B}T)^{-2}}$.

APPENDIX F: ENVELOPE OF CHARGE AND FLUX PROBABILITY DISTRIBUTIONS

In this appendix, we show that the envelope of the charge and flux probability distributions for stabilized states in the system are approximately given by Gaussians of standard deviations κe and $\kappa\varphi_0$, respectively, where

$$\kappa \equiv \frac{\sqrt{\coth(2\varepsilon_0/k_\mathrm{B}T)}}{\pi\lambda_0}, \qquad \lambda_0 \equiv \left(\frac{h f_{LC}}{4\pi^3 E_J}\right)^{1/4}. \tag{F1}$$

To obtain this result, it is convenient to first consider the charge probability density of a stabilized state, convolved with a Gaussian smoothening kernel of some given width σ,

$$\hat{W}_\sigma(q_0) = \frac{1}{\sqrt{2\pi}\sigma}\int_{-\infty}^{\infty} dq_1 e^{-(q_1-q_0)^2/2\sigma^2}\delta(\hat{q} - q_1), \tag{F2}$$

where $\hat{q}$ is the charge operator; here, we have introduced the $\hat{\cdot}$ accent to avoid confusion between operators and scalars. The above definition implies that $\langle \hat{W}_\sigma(q_0)\rangle = 1/\sqrt{2\pi}\sigma \int dq_1 e^{-(q_1-q_0)^2/2\sigma^2} p_q(q_1)$, where $p_q(x) = \langle \delta(\hat{q} - x)\rangle$ is the charge probability distribution of the system. In this sense, $\mathrm{Tr}[\hat{\rho}\hat{W}_\sigma(q_0)]$ gives the charge probability distribution in the state $\hat{\rho}$, when smoothed by a Gaussian kernel of width σ.

We now compute $\langle \hat{W}_\sigma(q)\rangle$ for a state stabilized by the protocol in the main text, $\hat{\rho}$. Below, we will exploit that stabilized states have all their φ support confined near integer multiples of φ_0. In order to do this, we first compute the matrix elements of $\hat{W}_\sigma(q)$ in the φ basis, $\{|\varphi\rangle\}$, where $|\varphi\rangle$ is the eigenstate of $\hat{\varphi}$ with eigenvalue φ and normalization $\langle\varphi|\varphi'\rangle = \delta(\varphi - \varphi')$. Using that $\langle\varphi|\delta(\hat{q} - q_1)|\varphi'\rangle = \frac{1}{2\pi\hbar}e^{-iq_1(\varphi-\varphi')/\hbar}$ in Eq. (F2) and completing the square leads us to

$$\langle\varphi|\hat{W}_\varphi(q_0)|\varphi'\rangle = \frac{1}{2\pi\hbar}e^{-i\frac{q_0}{\hbar}(\varphi-\varphi') - \frac{(\varphi-\varphi')^2}{2\Delta\varphi_\sigma}}, \tag{F3}$$

where $\Delta\varphi_\sigma \equiv \hbar/\sigma$. When $\sigma \gg e$, $\Delta\varphi_\sigma$ is much smaller than $\hbar/e = \varphi_0/\pi$. As a result, $\langle\varphi|\hat{W}_\varphi(q_0)|\varphi'\rangle$ is only nonzero when $|\varphi - \varphi_0| \ll \varphi_0$. Since $\langle\varphi|\hat{\rho}|\varphi'\rangle$ is only nonzero if φ and φ' are within a distance of approximately $\lambda\varphi_0$ from multiples of φ_0, we thus find that

$$\langle\hat{W}_\sigma(q)\rangle = \sum_z \int_{-[z+\frac{1}{2}]\varphi_0}^{[z+\frac{1}{2}]\varphi_0} d^2\varphi \langle\varphi|\hat{\rho}|\varphi'\rangle e^{-\frac{(\varphi-\varphi')^2}{2\Delta\varphi_\sigma^2} - i\frac{q_0}{\hbar}(\varphi-\varphi')}, \tag{F4}$$

with the shorthand $\int_a^b d^2\varphi = \int_a^b d\varphi \int_a^b d\varphi'$. This result holds for $\sigma \gg e$ and $\lambda \ll 1$. We recognize the above integral as

$$\int_{-\infty}^{\infty} d^2\varphi \langle\varphi|\hat{\rho}_z|\varphi'\rangle e^{-\frac{(\varphi-\varphi')^2}{2\Delta\varphi_\sigma^2} - i\frac{q_0}{\hbar}(\varphi-\varphi')},$$

where $\hat{\rho}_z$ is the projection of $\hat{\rho}$ into well z, defined as the φ interval $[z - 1/2]\varphi_0 < \hat{\varphi} < [z + 1/2\varphi_0]$. Using Eq. (F3), we can rewrite the integral as $1/2\pi\hbar \sum_z \mathrm{Tr}[W_\sigma(q)\rho_z]$, leading us to

$$\langle\hat{W}_\sigma(q_0)\rangle = \frac{1}{2\pi\hbar}\sum_z \mathrm{Tr}[W_\sigma(q)\rho_z]. \tag{F5}$$

We next recall that ρ_z describes the thermal steady state of a harmonic oscillator of vacuum fluctuation length λ_0 and excitation energy ε_0 (weighted by the total probability of finding the system in well z, $p_z \equiv \mathrm{Tr}[\rho_z]$). The charge probability distribution for this state is given by

$$\mathrm{Tr}[\hat{\rho}_z\delta(\hat{q} - q_1)] \approx \frac{p_z}{\sqrt{\pi}e\kappa}e^{-\frac{q_1^2}{\kappa^2 e^2}}. \tag{F6}$$

Combining Eqs. (F6) and (F2), and using the convolution rule for Gaussian distributions, we find that

$$\mathrm{Tr}[\hat{W}_\sigma(q)\hat{\rho}_z] = \frac{p_z}{\sqrt{\pi[2\sigma^2 + \kappa^2 e^2]}}e^{-\frac{q^2}{\kappa_\mathrm{th}^2 e + 2\sigma^2}}. \tag{F7}$$

Inserting this into Eq. (F5) and using $\sum_z p_z = 1$, we finally obtain

$$\langle\hat{W}_\sigma(q)\rangle \approx \frac{1}{\sqrt{2\pi[\kappa^2 e^2/2 + \sigma^2]}}e^{-\frac{q^2}{\kappa^2 e^2 + 2\sigma^2}}. \tag{F8}$$

Recalling the convolution rules for Gaussian distribution, this result is consistent with the envelope function for the charge distribution being given by a Gaussian with width κe.

To infer the envelope of the flux probability distribution, we note that this envelope is given by that of the charge probability distribution, after the rescaling $q/e \to \varphi/\varphi_0$; thus, the envelope of the flux probability distribution is a Gaussian of width $\kappa\varphi_0$.

APPENDIX G: EMERGENCE OF PEAK STRUCTURE IN THE CHARGE PROBABILITY DISTRIBUTION

Here, we demonstrate how the characteristic fractal peak structure of the charge probability distribution in Fig. 5 emerges—leveraged in the readout protocol discussed in Sec. VI.

When dissipatively stabilized, the system will initially be in a thermal mixture of coherent superpositions of low-energy states of the wells of the cosine potential from the Josephson junction. We consider one of such superpositions, writing it as $|\psi(0)\rangle = \sum_{m,\mu} c_{m\mu}|m,\mu\rangle$, where $|m,\mu\rangle$ is the state with wave function $\langle\varphi|m,\mu\rangle = \psi_\mu(\varphi - m\varphi_0)$, with

$$\psi_\mu(\varphi) \equiv e^{-\frac{\varphi^2}{2\lambda_0^2\varphi_0^2}} H_\mu\left(\varphi/\lambda_0\varphi_0\right)\left(2^\mu \mu! 2\pi\lambda_0\sqrt{\pi}\right)^{-1/2},$$

where $H_\mu(x)$ denotes the μth Hermite polynomial, i.e., the μth excited state of the harmonic oscillator corresponding to well m. For superpositions of low-energy-well states, $c_{m,\mu}$ is only nonzero for $\mu \ll \sqrt{1/\lambda_0}$. Note also that $c_{m\mu}$ is nonzero only for even or odd m when the system is in an $+1$ or -1 eigenstate of σ_z, respectively. Since the system is dissipatively stabilized, $\langle S_2\rangle \approx 1$, and the superposition is phase coherent: $c_{m\mu} \approx c_{m+2,\mu}$.

We now consider the evolution of $|\psi(0)\rangle$ during the stabilizer segment (neglecting the effects of dissipation, which can be analyzed via the approach from Sec. IV). After evolution with H_s for a time t, the state of the system is hence given by $e^{-iH_st}|\psi(0)\rangle \approx \sum_m c_{m\mu} e^{-i[m^2\varepsilon_L + \mu\varepsilon_0]t/\hbar}|m,\mu\rangle$.

To obtain the charge probability distribution, we consider the evolution of the Wigner function of the system, $W(\varphi,q,t) \equiv 1/\pi\hbar\int_{-\infty}^{\infty} d\varphi'\,\langle\varphi+\varphi'|\rho(t)|\varphi-\varphi'\rangle e^{2iq\varphi/\hbar}$, from which we may obtain the charge probability distribution through $p(q,t) = \int d\varphi W(\varphi,q,t)$. A straightforward derivation shows that

$$W(\varphi,q,t) = \sum_{m,n,\mu,\eta} c^*_{m\mu}c_{n\eta}e^{\pi i\frac{q(m-n)}{e} + i[\varepsilon_L(m^2-n^2)+\varepsilon_0(\mu-\eta)]t/\hbar} w_{\mu\eta} \times \left(\frac{\varphi - \varphi_0(k+l)}{2}, q\right), \tag{G1}$$

where $w_{\mu\eta}(\phi,q)$ is the cross-term Wigner function of eigenstates μ and η of the harmonic oscillator corresponding to the central well:

$$w_{\mu\eta}(\varphi,q) = \frac{1}{\pi\hbar}\int_{-\infty}^{\infty} d\varphi\,\psi^*_\mu(\varphi+\varphi')\psi_\eta(\varphi-\varphi')e^{2iq\varphi'/\hbar}. \tag{G2}$$

Introducing $l = m+n$, such that $(m^2-n^2) = l(l-2n)$, along with $\varepsilon_L = \pi\hbar 2\pi f_{LC}/2$, we find that

$$W(\varphi,q,t) = \sum_{l\in\mathbb{Z}}\sum_{\mu,\eta} e^{-i\varepsilon_0(\mu-\eta)t/\hbar} w_{\mu\eta}(\varphi - l\varphi_0/2, q) f_l^{\,\mu\eta} \times \left(q - le\frac{2\pi f_{LC}t}{2}\right), \quad f_l^{\,\mu\eta}(q) \equiv \sum_n c^*_{l-n,\mu}c_{n,\eta}\,e^{-\pi iq(l-2n)/e}. \tag{G3}$$

Since $c_{n,\mu} \approx c_{n+2,\mu}$, each $f_n^{\,\mu\eta}(q)$ is sharply peaked around $q \approx ze$ for $z \in \mathbb{Z}$; i.e., each $f_n(q)$ is a nascent Dirac comb with periodicity e. Since c_l is only nonzero when $l = s \bmod 2$, the sign of the peaks alternate based on the parity of n. Since $w_{\mu\eta}(\phi,q)$ is sharply peaked around $\phi = 0$, $W(\phi,q,0)$ has its support confined as peaks near $(\varphi,q) = (n_1\varphi_0/2, n_2e/2)$ for integer n_1 and n_2, with corresponding sign $(-1)^{(s+n_1)n_2}$. This grid structure is clearly visible in Fig. 5(b), where we plot the Wigner function numerically obtained for the system in Fig. 5(a) at $t = 0$. As t increases [see Eq. (G3)], the column of peaks where $\varphi = \varphi_0 n_1$ shifts in the positive q direction with velocity $\pi n_1 e f_{LC}$.

When $t = a/b(\tau_{LC}/2\pi)$ for integers a and b, peaks from columns where $an_1 \sim c\ (\bmod\ b)$ align at values $q/e = c/2b$. Thus, the charge probability distribution, $p(q,t) = \int d\varphi W(\varphi,q,t)$, has its support confined around values $q = ec/2b$ for each integer c. However, due to the alternating sign of peaks in columns where n_1 and s have opposite parities, the peaks of the Wigner function will only interfere constructively at values of c with parity s, provided that b is even. This interference is indicated with the dashed arrows in Fig. 5(a) at $t = \tau_{LC}/8\pi$. Consequently, $p(q,t)$ consists of peaks centered at values $q/e = (2n+s)/b$ where $n \in \mathbb{Z}$.

---

[1] P. W. Shor, Scheme for reducing decoherence in quantum computer memory, Phys. Rev. A **52**, R2493 (1995).

[2] A. R. Calderbank and P. W. Shor, Good quantum error-correcting codes exist, Phys. Rev. A **54**, 1098 (1996).

[3] A. M. Steane, Error correcting codes in quantum theory, Phys. Rev. Lett. **77**, 793 (1996).

[4] E. Knill, R. Laflamme, and W. H. Zurek, Resilient quantum computation, Science **279**, 342 (1998).

[5] R. Raussendorf and J. Harrington, Fault-tolerant quantum computation with high threshold in two dimensions, Phys. Rev. Lett. **98**, 190504 (2007).

[6] A. G. Fowler, M. Mariantoni, J. M. Martinis, and A. N. Cleland, Surface codes: Towards practical large-scale quantum computation, Phys. Rev. A **86**, 032324 (2012).

[7] R. Acharya *et al.*, (Google Quantum AI), Suppressing quantum errors by scaling a surface code logical qubit, Nature **614**, 676 (2023).

[8] B. M. Terhal, Quantum error correction for quantum memories, Rev. Mod. Phys. **87**, 307 (2015).

[9] J. Preskill, Quantum computing in the NISQ era and beyond, Quantum **2**, 79 (2018).

[10] S. J. Pauka, K. Das, R. Kalra, A. Moini, Y. Yang, M. Trainer, A. Bousquet, C. Cantaloube, N. Dick, G. C. Gardner, M. J. Manfra, and D. J. Reilly, A cryogenic CMOS chip for generating control signals for multiple qubits, Nat. Electron. **4**, 64 (2021).

[11] S. Bravyi and B. Terhal, A no-go theorem for a two-dimensional self-correcting quantum memory based on stabilizer codes, New J. Phys. **11**, 043029 (2009).

[12] H. Bombin, R. W. Chhajlany, M. Horodecki, and M. A. Martin-Delgado, Self-correcting quantum computers, New J. Phys. **15**, 055023 (2013), publisher: IOP Publishing.

[13] J. P. Barnes and W. S. Warren, Automatic quantum error correction, Phys. Rev. Lett. **85**, 856 (2000).

[14] B. Kraus, H. P. Büchler, S. Diehl, A. Kantian, A. Micheli, and P. Zoller, Preparation of entangled states by quantum Markov processes, Phys. Rev. A **78**, 042307 (2008).

[15] F. Verstraete, M. M. Wolf, and J. Ignacio Cirac, Quantum computation and quantum-state engineering driven by dissipation, Nat. Phys. **5**, 633 (2009).

[16] Z. Leghtas, G. Kirchmair, B. Vlastakis, R. J. Schoelkopf, M. H. Devoret, and M. Mirrahimi, Hardware-efficient autonomous quantum memory protection, Phys. Rev. Lett. **111**, 120501 (2013).

[17] F. Reiter, A. S. Sørensen, P. Zoller, and C. A. Muschik, Dissipative quantum error correction and application to quantum sensing with trapped ions, Nat. Commun. **8**, 1822 (2017).

[18] S. Touzard, A. Grimm, Z. Leghtas, S. O. Mundhada, P. Reinhold, C. Axline, M. Reagor, K. Chou, J. Blumoff, K. M. Sliwa, S. Shankar, L. Frunzio, R. J. Schoelkopf, M. Mirrahimi, and M. H. Devoret, Coherent oscillations inside a quantum manifold stabilized by dissipation, Phys. Rev. X **8**, 021005 (2018).

[19] C. Flühmann, T. L. Nguyen, M. Marinelli, V. Negnevitsky, K. Mehta, and J. P. Home, Encoding a qubit in a trapped-ion mechanical oscillator, Nature **566**, 513 (2019).

[20] D. R. Pérez and E. Kapit, Improved autonomous error correction using variable dissipation in small logical qubit architectures, Quantum Sci. Technol. **6**, 015006 (2020), publisher: IOP Publishing.

[21] P. M. Harrington, E. J. Mueller, and K. W. Murch, Engineered dissipation for quantum information science, Nat. Rev. Phys. **4**, 660 (2022).

[22] A. Grimm, N. E. Frattini, S. Puri, S. O. Mundhada, S. Touzard, M. Mirrahimi, S. M. Girvin, S. Shankar, and M. H. Devoret, Stabilization and operation of a Kerr-cat qubit, Nature **584**, 205 (2020), number: 7820 Publisher: Nature Publishing Group.

[23] A. Gyenis, A. Di Paolo, J. Koch, A. Blais, A. A. Houck, and D. I. Schuster, Moving beyond the transmon: Noise-protected superconducting quantum circuits, PRX Quantum **2**, 030101 (2021).

[24] B. Neeve, T.-L. Nguyen, T. Behrle, and J. P. Home, Error correction of a logical grid state qubit by dissipative pumping, Nat. Phys. **18**, 296 (2022).

[25] L.-A. Sellem, A. Sarlette, Z. Leghtas, M. Mirrahimi, P. Rouchon, and P. Campagne-Ibarcq, Dissipative protection of a GKP qubit in a high-impedance superconducting circuit driven by a microwave frequency comb, Phys. Rev. X **15**, 011011 (2025).

[26] D. Gottesman, A. Kitaev, and J. Preskill, Encoding a qubit in an oscillator, Phys. Rev. A **64**, 012310 (2001).

[27] J. Conrad, A. G. Burchards, and S. T. Flammia, Lattices, gates, and curves: GKP codes as a Rosetta stone, ArXiv:2407.03270.

[28] Note that our protocol does not directly generate a magic H state by projecting the LC oscillator vacuum state into the code subspace, as proposed in Ref. [103], since the nontrivial evolution toward the code subspace generated during by our stabilization protocol is inequivalent to a projection.

[29] P. Manset, J. Palomo, A. Schmitt, K. Gerashchenko, R. Rousseau, H. Patange, P. Abgrall, E. Flurin, S. Deléglise, T. Jacqmin, and L. Balembois, Hyperinductance based on stacked Josephson junctions, ArXiv:2505.02764.

[30] E. Afshari and A. Hajimiri, Nonlinear transmission lines for pulse shaping in silicon, IEEE J. Solid-State Circuits **40**, 744 (2005), conference Name: IEEE Journal of Solid-State Circuits.

[31] P. Campagne-Ibarcq, A. Eickbusch, S. Touzard, E. Zalys-Geller, N. E. Frattini, V. V. Sivak, P. Reinhold, S. Puri, S. Shankar, R. J. Schoelkopf, L. Frunzio, M. Mirrahimi, and M. H. Devoret, Quantum error correction of a qubit encoded in grid states of an oscillator, Nature **584**, 368 (2020), number: 7821 Publisher: Nature Publishing Group.

[32] A. Eickbusch, V. Sivak, A. Z. Ding, S. S. Elder, S. R. Jha, J. Venkatraman, B. Royer, S. M. Girvin, R. J. Schoelkopf, and M. H. Devoret, Fast universal control of an oscillator with weak dispersive coupling to a qubit, Nat. Phys. **18**, 1464 (2022).

[33] V. V. Sivak, A. Eickbusch, B. Royer, S. Singh, I. Tsioutsios, S. Ganjam, A. Miano, B. L. Brock, A. Z. Ding, L. Frunzio, S. M. Girvin, R. J. Schoelkopf, and M. H. Devoret, Real-time quantum error correction beyond break-even, Nature **616**, 50 (2023).

[34] D. Lachance-Quirion, M.-A. Lemonde, J. O. Simoneau, L. St-Jean, P. Lemieux, S. Turcotte, W. Wright, A. Lacroix, J. Fréchette-Viens, R. Shillito, F. Hopfmueller, M. Tremblay, N. E. Frattini, J. C. Lemyre, and P. St-Jean, Autonomous quantum error correction of Gottesman-Kitaev-Preskill states, Phys. Rev. Lett. **132**, 150607 (2024).

[35] X. C. Kolesnikow, R. W. Bomantara, A. C. Doherty, and A. L. Grimsmo, Gottesman-Kitaev-Preskill state

preparation using periodic driving, Phys. Rev. Lett. **132,** 130605 (2024).

[36] J. Conrad, Twirling and Hamiltonian engineering via dynamical decoupling for Gottesman-Kitaev-Preskill quantum computing, Phys. Rev. A **103,** 022404 (2021).

[37] M. Rymarz, S. Bosco, A. Ciani, and D. P. DiVincenzo, Hardware-encoding grid states in a nonreciprocal superconducting circuit, Phys. Rev. X **11,** 011032 (2021).

[38] The operator $\Xi(\varphi/\varphi_0)$ may conveniently be computed as $\sum_n c_n e^{-\pi in\varphi/\varphi_0}$, where the $\{c_n\}$ are the Fourier coefficients of Ξ. Note that c_n is only nonzero for odd n due to the antisymmetry $\Xi(x) = -\Xi(x+1)$.

[39] G. Pantaleoni, B. Q. Baragiola, and N. C. Menicucci, Modular bosonic subsystem codes, Phys. Rev. Lett. **125,** 040501 (2020).

[40] Y. Ouyang and E. T. Campbell, Trade-offs on number and phase shift resilience in bosonic quantum codes, IEEE Trans. Inf. Theory **67,** 6644 (2021).

[41] M. Mirrahimi, Z. Leghtas, V. V. Albert, S. Touzard, R. J. Schoelkopf, L. Jiang, and M. H. Devoret, Dynamically protected cat-qubits: A new paradigm for universal quantum computation, New J. Phys. **16,** 045014 (2014), publisher: IOP Publishing.

[42] M. H. Michael, M. Silveri, R. T. Brierley, V. V. Albert, J. Salmilehto, L. Jiang, and S. M. Girvin, New class of quantum error-correcting codes for a bosonic mode, Phys. Rev. X **6,** 031006 (2016).

[43] M. V. Larsen *et al.*, Integrated photonic source of Gottesman-Kitaev-Preskill qubits, Nature **642,** 587 (2025), publisher: Nature Publishing Group.

[44] M. Holthaus and M. E. Flatté, Subharmonic generation in quantum systems, Phys. Lett. A **187,** 151 (1994).

[45] K. Sacha, Modeling spontaneous breaking of time-translation symmetry, Phys. Rev. A **91,** 033617 (2015).

[46] V. Khemani, A. Lazarides, R. Moessner, and S. L. Sondhi, Phase structure of driven quantum systems, Phys. Rev. Lett. **116,** 250401 (2016).

[47] D. V. Else, B. Bauer, and C. Nayak, Floquet time crystals, Phys. Rev. Lett. **117,** 090402 (2016).

[48] Y. Zhang, J. Gosner, S. M. Girvin, J. Ankerhold, and M. I. Dykman, Time-translation-symmetry breaking in a driven oscillator: From the quantum coherent to the incoherent regime, Phys. Rev. A **96,** 052124 (2017).

[49] Z. Gong, R. Hamazaki, and M. Ueda, Discrete time-crystalline order in cavity and circuit QED systems, Phys. Rev. Lett. **120,** 040404 (2018).

[50] N. Lörch, Y. Zhang, C. Bruder, and M. I. Dykman, Quantum state preparation for coupled period tripling oscillators, Phys. Rev. Res. **1,** 023023 (2019).

[51] F. Nathan, G. Refael, M. S. Rudner, and I. Martin, Quantum frequency locking and downconversion in a driven qubit-cavity system, Phys. Rev. Res. **2,** 043411 (2020).

[52] H. P. Breuer and F. Petruccione, *The Theory of Open Quantum Systems* (Oxford University Press, Oxford, United Kingdom, 2002).

[53] C. Gardiner and P. Zoller, *Quantum Noise* (Springer-Verlag, Berlin, 2004).

[54] F. Nathan and M. S. Rudner, Universal Lindblad equation for open quantum systems, Phys. Rev. B **102,** 115109 (2020).

[55] J. Ankerhold, H. Grabert, and G.-L. Ingold, Dissipative quantum systems with a potential barrier: General theory and the parabolic barrier, Phys. Rev. E **51**, 4267 (1995).

[56] Specifically, $H_{\rm rf}$ is defined such that $\partial_t V^\dagger \rho V = -i[H_{\rm rf}, V^\dagger \rho V]$.

[57] This result can, e.g., be seen by noting that $\bar{\varphi}$ is a φ_0-periodic function of φ and thus can be written as $\bar{\varphi} = \sum_n c_n e^{-2\pi in\varphi/\varphi_0}$ for some coefficients $\{c_n\}$. Since $e^{-2\pi in\varphi/\varphi_0}$ translates q by $2en$, we see that $e^{2\pi in\varphi/\varphi_0}, S_2 = 0$, and hence also $\bar{\varphi}, S_2 = 0$.

[58] This may, e.g., be defined such that $\rho(t)$ has its $\bar{\varphi}$ support confined in the interval $|\bar{\varphi}| \leq \Delta\varphi(t)$, up to a residual weight given by some exponentially small error tolerance $\delta p \ll 1$ which we specify. Due to the Gaussian envelope of the probability support in each well, $\Delta\varphi(t)$ can be significantly smaller than $\varphi_0/2$ even when we pick δp exponentially small.

[59] More precisely, with the definition of $\Delta\varphi$ in note [58], the evolution of $\tilde{\rho}(t)$ is unaffected up to (exponentially suppressed) δp corrections if we replace $\bar{\varphi}$ with the time-dependent operator $\bar{\varphi}_c(t)$ in Eq. (17), where $\bar{\varphi}(t) = \bar{\varphi}$ for $|\bar{\varphi}| \leq \Delta\varphi(t)$ and $\bar{\varphi}_c(t) = \Delta\varphi(t)$ for $|\bar{\varphi}| \geq \Delta\varphi(t)$.

[60] For instance, with the trunctation scheme in note [59], it would relax to $c\lambda\varphi_0$, where c is the $\mathcal{O}(1)$ cutoff scale introduced there.

[61] Specifically, $\mathcal{S}_{ij} = \delta_{iz}\delta_{jz} + \epsilon_{ijz}$, where ϵ_{ijk} is the Levi-Civita symbol.

[62] To see this, note that for $z \in \mathbb{Z}$ and $|\delta\varphi| \leq \varphi_0/2$, $\bar{\sigma}_x|z\varphi_0 + \delta\varphi\rangle = |-(z-1)\varphi_0 + \delta\varphi\rangle$ and $\bar{\sigma}_z|z\varphi_0 + \delta\varphi\rangle = (-1)^z|z\varphi_0 + \delta\varphi\rangle$. Noting that the states $|z\varphi_0 + \delta\varphi\rangle$ form a complete orthormal basis, the above relations imply that $\bar{\sigma}_x^2 = \bar{\sigma}_z^2 = 1$ and $\bar{\sigma}_x\bar{\sigma}_z = -\bar{\sigma}_z\bar{\sigma}_x$, implying that the anticommutator relations hold.

[63] This T gate is the Hermitian conjugate of the usual definition of the T gate, which would assign a $e^{-i\pi/8}$ phase to logical $|0\rangle$ states relative to logical $|1\rangle$ states. The gate is exponentially protected by the same mechanism as the S gate for the configuration discussed in the previous sections.

[64] S. Danilin, A. V. Lebedev, A. Vepsäläinen, G. B. Lesovik, G. Blatter, and G. S. Paraoanu, Quantum-enhanced magnetometry by phase estimation algorithms with a single artificial atom, npj Quantum Inf. **4,** 29 (2018).

[65] R. P. Budoyo, K. Kakuyanagi, H. Toida, Y. Matsuzaki, and S. Saito, Electron spin resonance with up to 20 spin sensitivity measured using a superconducting flux qubit, Appl. Phys. Lett. **116**, 194001 (2020).

[66] The initial state consisted of well ground states with a Gaussian envelope and had wave function $\Psi_s(\varphi)$ for $s = 0, 1$, where $\Psi_s(\varphi) = \sum_k e^{-8\pi^2{\lambda_0}^2k^2} e^{-(\varphi-[2k+s]\varphi_0)/2{\lambda_0}^2\varphi_0^2}$ (up to a normalization).

[67] A. Isar, W. Scheid, and A. Sandulescu, Quasiprobability distributions for open quantum systems within the Lindblad theory, J. Math. Phys. **32**, 2128 (1991).

[68] The inverse scaling with f_{LC} arises due to the parametrization we use for charge noise: the coupling between system and charge noise is proportional to C^{-2} while $C \propto f_{LC}^{-1}$, due to Eq. (5) fixing the resonator impedance. The charge-noise-induced diffusion rate thus scales with f_{LC}^2 for fixed γ_q, while the tolerance for the diffusion rate scales with

f_{LC}^{-1}. As a result, smaller f_{LC} leads to more stability with our parametrization.

[69] G. Kiršanskas, M. Franckié, and A. Wacker, Phenomenological position and energy resolving Lindblad approach to quantum kinetics, Phys. Rev. B **97**, 035432 (2018).

[70] F. Nathan, Ph.D. Thesis, Niels Bohr Institute, University of Copenhagen, 2018.

[71] F. Nathan, I. Martin, and G. Refael, Topological frequency conversion in a driven dissipative quantum cavity, Phys. Rev. B **99**, 094311 (2019).

[72] D. Davidović, Geometric-arithmetic master equation in large and fast open quantum systems, J. Phys. A: Math. Theor. **55**, 455301 (2022).

[73] F. Nathan and M. S. Rudner, Quantifying the accuracy of steady states obtained from the universal Lindblad equation, Phys. Rev. B **109**, 205140 (2024).

[74] Here, we have used that $\varepsilon_0 = 4\pi {\lambda_0}^2 E_J$.

[75] J. Dalibard, Y. Castin, and K. Mølmer, Wave-function approach to dissipative processes in quantum optics, Phys. Rev. Lett. **68**, 580 (1992).

[76] H. Carmichael, *An Open Systems Approach to Quantum Optics* (Springer Berlin, Heidelberg, 1993).

[77] Specifically, we initialize the system in a state with wave function $\Psi_0(\varphi) = \sum_{n=-45}^{45} \sum_{k=0}^{35} c_{nk} \psi_k(\varphi - n\varphi_0)$, with $\psi_k(\varphi)$ the kth harmonic oscillator eigenstate with vacuum fluctuation width $\lambda_0\varphi_0$ (see Fig. 4), and $\{c_{nk}\}$ random complex numbers with zero mean and identical variances.

[78] Specifically, the system has been initialized in a superposition of Gaussian wave functions with a Gaussian envelope, with the wave function $\Psi(\varphi) = \cos\left(\frac{\theta}{2}\right) \Psi_0(\varphi) + \sin\left(\frac{\theta}{2}\right) e^{i\varphi} \Psi_1(\varphi)$, where $\Psi_s(\varphi) = \mathcal{N} \sum_k e^{-(2k+s)^2\pi^2{\lambda_0}^2/4}$ $e^{-(\varphi-[2k+s]\varphi_0)^2/2{\lambda_0}^2\varphi_0^2}$, with $\mathcal{N}$ a normalization constant and $(\theta, \phi) = (1.93, 1.62)$ chosen randomly on the unit sphere. The state above is well confined in the code subspace and realizes the logical state $\cos\left(\frac{\theta}{2}\right)|0\rangle + \sin\left(\frac{\theta}{2}\right) e^{i\varphi}|1\rangle$. We also note that the results do not rely on the particular details of the initialization, except for the initial expectation values of the logical operators. After a few cycles of the protocol, the resonator has reached a thermal ensemble of generalized GKP states with no memory of the initialization, except for the initially encoded logical information.

[79] Due to the long qubit lifetime in this regime, the level of decay that we can resolve on the simulated timescale is very small and thus subject to significant statistical fluctuations between SSE trajectories. To overcome this, we show time-coarse-grained data, obtained by time-averaging the Bloch-vector length over 400 driving periods. We also use the time-coarse-grained data for our fit. We have confirmed that the lifetime fit varies little with the chosen window length, while the quality of the linear fit increases with n.

[80] We speculate that the near-stationary interval arises from a small effective Lieb-Robinson velocity in phase space, which implies that it takes a long time for exponential tails of the phase-space support of the state to spread to the domain boundaries of the logical operators.

[81] The values of $\log \|\langle \boldsymbol{\sigma} \rangle\|^2$ shown in Fig. 7(d) are very small and hence the logarithm can be well approximated by its first-order Taylor series over this range of values. Thus, $\log \|\langle \boldsymbol{\sigma} \rangle\|^2$ being linear over this range is not conclusive evidence that the Bloch-vector length decays exponentially in time; nonetheless, the inverse slope still defines a meaningful lifetime for the qubit.

[82] I. V. Pechenezhskiy, R. A. Mencia, L. B. Nguyen, Y.-H. Lin, and V. E. Manucharyan, The superconducting quasicharge qubit, Nature **585**, 368 (2020).

[83] M. Peruzzo, A. Trioni, F. Hassani, M. Zemlicka, and J. M. Fink, Surpassing the resistance quantum with a geometric superinductor, Phys. Rev. Appl. **14**, 044055 (2020).

[84] W. C. Smith, M. Villiers, A. Marquet, J. Palomo, M. R. Delbecq, T. Kontos, P. Campagne-Ibarcq, B. Douçot, and Z. Leghtas, Magnifying quantum phase fluctuations with Cooper-pair pairing, Phys. Rev. X **12**, 021002 (2022).

[85] A. Anferov, F. Wan, S. P. Harvey, J. Simon, and D. I. Schuster, Millimeter-wave superconducting qubit, PRX Quantum **6**, 020336 (2025).

[86] L. Casparis, M. R. Connolly, M. Kjaergaard, N. J. Pearson, A. Kringhøj, T. W. Larsen, F. Kuemmeth, T. Wang, C. Thomas, S. Gronin, G. C. Gardner, M. J. Manfra, C. M. Marcus, and K. D. Petersson, Superconducting gatemon qubit based on a proximitized two-dimensional electron gas, Nat. Nanotechnol. **13**, 915 (2018), number: 10 Publisher: Nature Publishing Group.

[87] M. Samizadeh Nikoo, A. Jafari, N. Perera, M. Zhu, G. Santoruvo, and E. Matioli, Nanoplasma-enabled picosecond switches for ultrafast electronics, Nature **579**, 534 (2020), publisher: Nature Publishing Group.

[88] A. Kemppinen, A. J. Manninen, M. Möttönen, J. J. Vartiainen, J. T. Peltonen, and J. P. Pekola, Suppression of the critical current of a balanced superconducting quantum interference device, Appl. Phys. Lett. **92**, 052110 (2008).

[89] Y. Lu, A. Maiti, J. W. O. Garmon, S. Ganjam, Y. Zhang, J. Claes, L. Frunzio, S. M. Girvin, and R. J. Schoelkopf, High-fidelity parametric beamsplitting with a parity-protected converter, Nat. Commun. **14**, 5767 (2023), publisher: Nature Publishing Group.

[90] R. Lescanne, M. Villiers, T. Peronnin, A. Sarlette, M. Delbecq, B. Huard, T. Kontos, M. Mirrahimi, and Z. Leghtas, Exponential suppression of bit-flips in a qubit encoded in an oscillator, Nat. Phys. **16**, 509 (2020), publisher: Nature Publishing Group.

[91] A. Vanselow, B. Beauseigneur, L. Lattier, M. Villiers, A. Denis, P. Morfin, Z. Leghtas, and P. Campagne-Ibarcq, Dissipating quartets of excitations in a superconducting circuit, ArXiv:2501.05960.

[92] M. Geier and F. Nathan, Self-correcting GKP qubit in a superconducting circuit with an oscillating voltage bias, ArXiv:2412.03650.

[93] L. Glazman and G. Catelani, Bogoliubov quasiparticles in superconducting qubits, SciPost Physics Lecture Notes, 31 (2021).

[94] R.-P. Riwar, A. Hosseinkhani, L. D. Burkhart, Y. Y. Gao, R. J. Schoelkopf, L. I. Glazman, and G. Catelani, Normal-metal quasiparticle traps for superconducting qubits, Phys. Rev. B **94**, 104516 (2016), publisher: American Physical Society.

[95] Google Quantum AI and Collaborators, Quantum error correction below the surface code threshold, Nature **638**, 920 (2025).

[96] Microsoft Azure Quantum, M. Aghaee *et al.*, Interferometric single-shot parity measurement in InAs-Al hybrid devices, Nature **638**, 651 (2025).

[97] For example, setting $w_0 = 6\kappa$ leads to an error of order $\mathrm{erfc}(6) \sim 10^{-17}$.

[98] This holds since $\|X\|_{\mathrm{tr}} = \|X^\dagger\|_{\mathrm{tr}}$, and $\|\mathcal{U}X\|_{\mathrm{tr}} = \|X\|_{\mathrm{tr}}$ for any unitary $\mathcal{U}$.

[99] The choice $k = k_0$ is chosen because it results in simple expressions for the bounds that we obtain. We emphasize that sharper bounds can possibly be obtained for different values of k.

[100] To see that the right-hand side is Hermitian, note that the $2e$ periodicity of $f_\alpha{}'(q/e)$ implies $[\bar{\varphi}, f_\alpha{}'(q/e)] = 0$.

[101] To see this, note that $\|AB\|_{\mathrm{tr}} = \mathrm{Tr}[\mathcal{U}AB]$ for some unitary $\mathcal{U}$ that generates the polar decomposition of AB. The result follows using $|\mathrm{Tr}(AB)| \leq \|A\|\|B\|_{\mathrm{tr}}$.

[102] Specifically, $\|\mathcal{O}\rho\|_{\mathrm{tr}} = \mathrm{Tr}[\mathcal{U}\mathcal{O}\rho]$ for some unitary $\mathcal{U}$ that generates the polar decompositon of $\mathcal{O}\rho$. We identify $\mathrm{Tr}[\mathcal{U}\mathcal{O}\rho] = (\sqrt{\rho}, \sqrt{\rho}\mathcal{U}\mathcal{O})_{\mathrm{HS}}$, where $(x, y)_{\mathrm{HS}} = \mathrm{Tr}[x^\dagger y]$ is the Hilbert-Schmidt inner product. The result follows when using the Cauchy-Schwartz inequality, $(x, y)_{\mathrm{HS}} \leq \sqrt{(x, x)_{\mathrm{HS}}(y, y)_{\mathrm{HS}}}$.

[103] B. Q. Baragiola, G. Pantaleoni, R. N. Alexander, A. Karanjai, and N. C. Menicucci, All-Gaussian universality and fault tolerance with the Gottesman-Kitaev-Preskill code, Phys. Rev. Lett. **123**, 200502 (2019).